The 2019-2020 Khalili (Iran) earthquake sequence - anthropogenic seismicity in the Zagros Simply Folded Belt?

Mohammadreza Jamalreyhani[1], Léa Pousse-Beltran[2], Pınar Büyükakpınar[3], Simone Cesca[4], Edwin Nissen[5], Abdolreza Ghods[6], José Ángel López-Comino[7], Mahdi Rezapour[8], and Mahdi Najafi[9]

[1]Institute of Geophysics, University of Tehran, Iran- GFZ German research center for Geosciences, Potsdam, Germany
[2]School of Earth and Ocean Sciences, University of Victoria, Victoria, British Columbia, Canada- Univ. Grenoble Alpes, Univ. Savoie Mont Blanc, CNRS, IRD, UGE, ISTerre, 38000 Grenoble, France
[3]Kandilli Observatory and Earthquake Research Institute, Boğaziçi University, İstanbul, Turkey
[4]GFZ German Research Centre for Geosciences
[5]University of Victoria
[6]Institute for Advanced Studies in Basic Sciences
[7]University of Granada
[8]Geophysics
[9]Department of Earth Sciences, Institute for Advanced Studies in Basic Sciences (IASBS), Zanjan, Iran

November 24, 2022

Abstract

We investigate the origin of a long-lived earthquake cluster in the Fars arc of the Zagros Simply Folded Belt that is co-located with the major Shanul natural gas field near the small settlement of Khalili. The cluster emerged in January 2019 and initially comprised small events of w 5.4 and 5.7 earthquakes, which were followed by > 100 aftershocks. We assess the spatio-temporal evolution of the earthquake sequence using multiple event hypocenter relocations, waveform inversions, and Sentinel-1 Interferometric Synthetic Aperture Radar (InSAR) measurements and models. We find that the early part of the sequence is spatially distinct from the June 9, 2020 earthquakes and their aftershocks. Moment tensors, centroid depths, and source parameter uncertainties of fifteen of the largest (Mn [?] 4.0) events show that the sequence is dominated by reverse faulting at shallow depths (mostly [?] 4 km) within the sedimentary cover. InSAR modelling shows that the Mw 5.7 mainshock occurred at depths of 2–8 km, with a rupture length and maximum slip of ~20 km and ~0.5 m, respectively. Our results strongly suggest that the 2019-2020 Khalili earthquake sequence was influenced by the operation of the Shanul field, making these the first known examples of gas extraction anthropogenic earthquakes in Zagros. Understanding the genesis of such events to distinguish man-made seismicity from natural earthquakes is helpful for hazard and risk assessment, notably in Iran which is both seismically-active and rich in oil and gas reserves.

The 2019–2020 Khalili (Iran) earthquake sequence — anthropogenic seismicity in the Zagros Simply Folded Belt?

Mohammdreza Jamalreyhani[1,2], Léa Pousse-Beltran[3,4], Pınar Büyükakpınar[5], Simone Cesca[2], Edwin Nissen[3], Abdolreza Ghods[6], José Ángel López-Comino[7,8,9], Mehdi Rezapour[1], Mahdi Najafi[6]

[1]Institute of Geophysics, University of Tehran, Iran.

[2]GFZ German research center for Geosciences, Potsdam, Germany.

[3]School of Earth and Ocean Sciences, University of Victoria, Victoria, British Columbia, Canada

[4]Univ. Grenoble Alpes, Univ. Savoie Mont Blanc, CNRS, IRD, UGE, ISTerre, 38000 Grenoble, France

[5]Kandilli Observatory and Earthquake Research Institute, Boğaziçi University, İstanbul, Turkey.

[6]Department of Earth Sciences, Institute for Advanced Studies in Basic Sciences, Zanjan, Iran.

[7]Instituto Andaluz de Geofísica, Universidad de Granada, Granada, Spain.

[8]Departamento de Física Teórica y del Cosmos, Universidad de Granada, Granada, Spain.

[9]Institute of Geosciences, University of Potsdam, Potsdam-Golm, Germany.

Corresponding author: Mohammadreza Jamalreyhani (m.jamalreyhani@gmail.com)

Key Points:

- Discrimination of anthropogenic earthquakes in areas of naturally-elevated seismicity is challenging.
- The 2019-2020 Khalili earthquake sequence is the first well-resolved example of induced seismicity linked to gas extraction in the Zagros.
- Understanding anthropogenic and natural seismicity is important in Iran which is both seismically-active and rich in hydrocarbon reserves.

Abstract

We investigate the origin of a long-lived earthquake cluster in the Fars arc of the Zagros Simply Folded Belt that is co-located with the major Shanul natural gas field near the small settlement of Khalili. The cluster emerged in January 2019 and initially comprised small events of *M*n ~3–4. It culminated on June 9, 2020 with a pair of *M*w 5.4 and 5.7 earthquakes, which were followed by > 100 aftershocks. We assess the spatio-temporal evolution of the earthquake sequence using multiple event hypocenter relocations, waveform inversions, and Sentinel-1 Interferometric Synthetic Aperture Radar (InSAR) measurements and models. We find that the early part of the sequence is spatially distinct from the June 9, 2020 earthquakes and their aftershocks. Moment tensors, centroid depths, and source parameter uncertainties of fifteen of the largest (*M*n ≥ 4.0) events show that the sequence is dominated by reverse faulting at shallow depths (mostly ≤ 4 km) within the sedimentary cover. InSAR modelling shows that the *M*w 5.7 mainshock occurred at depths of 2–8 km, with a rupture length and maximum slip of ~20 km and ~0.5 m, respectively. Our results strongly suggest that the 2019-2020 Khalili earthquake sequence was influenced by the operation of the Shanul field, making these the first known examples of gas extraction anthropogenic earthquakes in Zagros. Understanding the genesis of such events to distinguish man-made seismicity from natural earthquakes is helpful for hazard and risk assessment, notably in Iran which is both seismically-active and rich in oil and gas reserves.

Plain Language Summary

Earthquakes caused by human activities have been documented in a growing number of regions worldwide, but recognizing these events in areas of naturally-elevated seismicity remains challenging. We investigate the origin of earthquake cluster in the Zagros mountains — one of the world's most seismically active mountain belts — that is co-located with a major natural gas field. The seismicity led to public concern and speculation that nearby natural gas extraction was responsible. We assess the spatio-temporal evolution of the earthquake sequence and use satellite geodesy and seismology measurements and models. Our results support these being the first, well-resolved examples of anthropogenic earthquakes related to gas extraction in the Zagros. We suggest that the exploitation of the reservoirs in Iran should be preceded by risk assessment studies and accompanied by the implementation of dedicated, sophisticated monitoring, which would allow seismicity to be detected early and tracked more closely.

1 Introduction

Anthropogenic earthquakes, defined as those induced or triggered by human actions, have now been identified in many different regions across the globe (Foulger et al., 2018). Activities known or suspected to cause anthropogenic seismicity include subsurface fluid injection or extraction — through hydraulic fracturing, geothermal energy exploitation, and gas storage — as well as mining operations and water reservoir impoundment (Grigoli et al., 2017; Foulger et al., 2018; Keranen & Weingarten, 2018).

These activities can introduce pore pressure transients and alter the local stress field, consequently promoting (or inhibiting) earthquake occurrence (Ellsworth 2013, Dahm et al., 2013). Fluid injection-induced seismicity (IIS) has become particularly widespread in recent years due to increased shale gas exploitation and waste water disposal, geothermal stimulation, and gas storage (Ellsworth 2013, Foulger et al., 2018). To date, IIS has reached moderate magnitudes — for example the 2017 M_w 5.5 Pohang earthquake (e.g. Grigoli et al., 2018), the

2016 M_w 5.1 Fairview, M_w 5.7 Prague, and M_w 5.8 Pawnee, Oklahoma earthquakes (Ellsworth 2013, Keranen et al., 2014, Yeck et al., 2017), and the 2013 M_w 4.3 earthquake in Castor gas storage (Cesca et al., 2014) — sufficient that there are often strong socioeconomic impacts (Grigoli et al., 2017).

Recognizing anthropogenic earthquakes is particularly challenging in regions of naturally-elevated seismicity, with detailed source analyses essential in order to discriminate between the two (Dahm et al., 2015). The Zagros fold-and-thrust belt within the Arabia-Eurasia collision zone (Figure 1a) offers an excellent example, comprising one of the most seismically-active mountain belts as well as one of the greatest loci of oil and gas production in the world. The outer part of the range, known as the Simply Folded Belt, is characterized by a thick (averaging ~10 km) sedimentary cover that contains hidden reverse faults that host frequent large, damaging earthquakes (e.g. Talebian & Jackson 2004; Nissen et al., 2011). The folded and faulted sediments contain 90% of Iran's proven hydrocarbon reservoirs including the world's second-largest gas reserves, estimated at ~32.0 trillion cubic meters, or ~17% of Earth's total. Having started gas production in 1990, Iran now produces more than one billion cubic meters of gas per day from 36 gas fields, most of which are located in the Fars arc in the south-eastern Zagros (Figure 1b; Esrafili-Dizaji & Rahimpour-Bonab, 2013; Vergés et al., 2011). Despite the intense hydrocarbon production, there have so far been no unequivocal cases of earthquakes linked to gas/oil extraction or waste-water disposal in the Zagros — though a few earthquakes have been attributed to reservoir impoundment (Kangi and Heidari, 2008), mining (Mansouri-Daneshvar et al., 2018) and groundwater pumping (Kundu et al., 2019).

Here, we investigate a prominent cluster of felt earthquakes near Khalili, in the central Fars arc, starting in January 2019. The swarm-like activity and its spatial association with the major Shanul gas field raised legitimate concerns of an anthropogenic cause. The sequence culminated in mid-2020 with a M_w 4.7 earthquake on May 31, M_w 5.4 and 5.7 earthquakes on June 9, and a sustained aftershock sequence. The largest event, at 17:18 UTC on June 9, was responsible for several injuries.

In this study, we present a detailed analysis of the Khalili sequence to gain insights into its mechanisms and origins. By utilizing stations of the Iranian Seismological Center seismic network (IRSC; see *Data availability*), which are denser here than in many other parts of Iran, we relocated the 18 month-long sequence and calculated focal mechanisms and centroid depths for the fifteen largest ($M_w > 4.0$) events. We also estimated the coseismic slip distribution of the June 9, 2020 M_w 5.7 mainshock using Interferometric Synthetic Aperture Radar (InSAR) measurements and elastic dislocation models. We compared the results with subsurface geology constructed using 2-D seismic profiles. Our results reveal a close spatial correlation between seismicity and extraction/injection operation in the Shanul gas field, as well as a number of anomalous source characteristics for the larger events. For the first time, we suggest a case of anthropogenic earthquakes related to gas extraction in the Zagros.

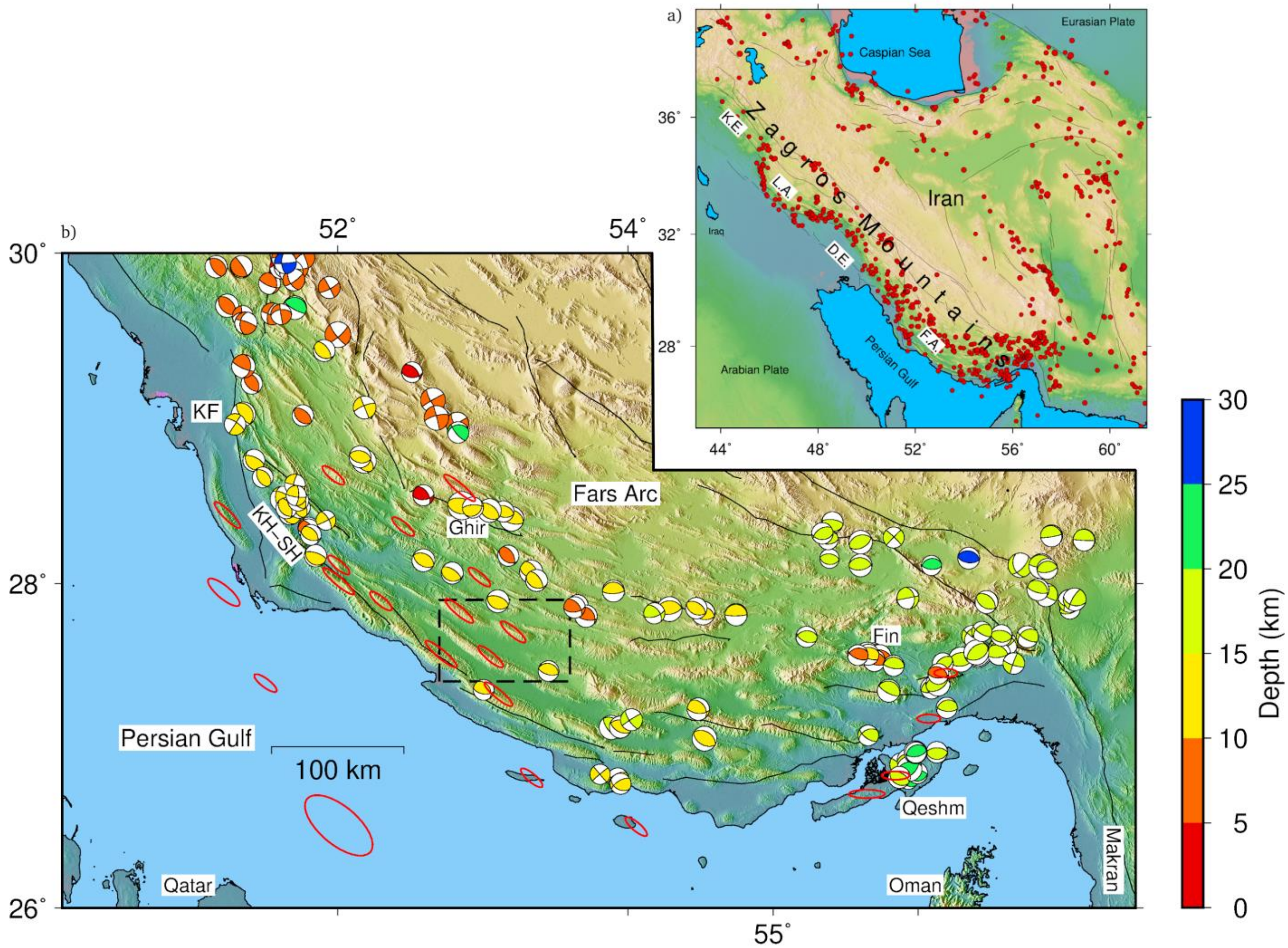

Figure 1. (a) Iranian seismicity, showing the location of the Zagros mountains at the leading edge of the Arabia-Eurasia collision zone. Red circles are *M* >5.0 earthquakes from 1900–2019 from the USGS catalog. The most active, outer part of the Zagros (simply folded belt) can be subdivided into four tectono-stratigraphic domains: from SE to NW, the Fars arc (F.A.), Dezful embayment (D.E.), Lurestan arc (L.A.), and the Kirkuk embayment (K.E.). **(b)** A zoom-in of the Fars arc. A large number of anticlines are evident in the topography, several of which contain active gas fields (red ellipses). Black lines show major mapped active faults, including the right-lateral Kazerun Fault (K.F.). Focal mechanisms from published waveform modeling studies are plotted at relocated epicenters and coloured according to focal depth (Karasözen et al., 2019 and references therein). Notable earthquake sequences include those at Khaki-Shonbe (KH–SH; Elliott et al., 2015), Ghir (e.g. Berberian, 1995), Fin (Roustaei et al., 2010), and Qeshm (Nissen et al., 2010, 2014; Lohman & Barnhart, 2010). The black rectangle shows our study area (Figure 2).

2 Background

2.1. Active tectonics, structure, and seismicity of the Fars arc

The Fars arc refers to the arcuate part of the southeastern Zagros between the Kazerun fault in the west and the Bandar Abbas syntaxis in the east (Figure 1b). GPS measurements indicate 10 mm/yr of NNE-directed convergence across the central Fars arc (e.g. Tatar et al., 2004). This shortening is manifest at the surface in symmetric, range-parallel folds with amplitudes of up to a few kilometers and wavelengths of ~10–20 km (e.g. Edey et al., 2020), and at depth in frequent earthquakes on steeply dipping (30°–60°), blind reverse faults (Berberian, 1995; Talebian & Jackson, 2004; Nissen et al., 2011). There are no known examples of coseismic surface rupture in the Fars arc, and the mechanical relationship between buried faults and surface folds remains a matter of debate.

The sedimentary cover of the Fars Arc is detached from the underlying basement by a layer of Ediacaran–early Cambrian Hormuz salt, which also surfaces in numerous diapirs (e.g. Jahani et al., 2009, 2017; Barnhart & Lohman 2012; Edey et al., 2020). Estimates of the depth of this interface vary from as little as ~6–8 km (e.g. Sherkati et al., 2005) to as great as ~14–20 km (Jahani et al., 2017). In the central Fars arc, closest to our study area, orogen-scale geological cross-sections interpret the basement depth to be ~8–12 km (e.g. Allen et al., 2013; Najafi et al., 2014). Analysis of local and teleseismic earthquakes collected in 1997 by a temporary (~2 month) dense seismological network in the Ghir region, ~100 km north of Khalili, resolved thicknesses of 11 km and 46 km for the sedimentary cover and crust, respectively (Tatar et al., 2004).

InSAR and teleseismic waveform modelling studies suggest that many of the larger (M_w > 5) earthquakes of the Fars arc are located within the so-called "Competent Group" of mechanicallystrong platform carbonates that make up the middle-to-lower sedimentary cover at depths of ~5–10 km (Nissen et al., 2010, 2011, 2014; Lohman & Barnhart 2010; Roustaei et al., 2010; Barnhart et al., 2013; Elliott et al., 2015). At the same time, a number of microseismic studies have indicated concentrations of small earthquakes at probable basement depths of ~10–20 km (e.g. Tatar et al., 2004; Nissen et al., 2011). Helping to reconcile these differences, a recent relocation of the 70-year catalog of well-recorded, moderate to large earthquakes indicated a focal depth range of 4–25 km (Karasözen et al., 2019). Till now, the largest instrumental earthquakes in the Fars arc have not exceeded M_w 6.7, reflecting that the seismogenic layer is segmented vertically by the Hormuz salt and other weak evaporitic or shale horizons within the cover, across which seismic rupture cannot propagate (Nissen et al., 2010). This mechanical segmentation also manifests itself in coseismic slip planes with characteristically narrow (small width-to-length ratio) dimensions (Roustaei et al., 2010; Elliott et al., 2015).

2.2. Geologic structure, production history, and background seismicity of the study area

The Shanul field is part of a concentration of natural gas reservoirs in the central and western Fars arc (Figure 1b). This region is characterized by symmetric to weakly-asymmetric “whaleback” folds with characteristic wavelengths of ~10–20 km and amplitudes of ~2–4 km, which are controlled primarily by detachment along the Hormuz salt at ~8–12 km depth (Allen et al., 2013; Motamedi et al., 2012; Najafi et al., 2014). Published seismic reflection imagery shows that many of the anticlines exhibit “pop-up” geometries accompanied by pairs of opposite-verging, high-angle reverse faults on both flanks, originating either from the Hormuz detachment at the base of the cover (Najafi et al., 2014) or a secondary decollement within Triassic Dashtak evaporites of the middle cover (Figure 2) (Motamedi et al., 2012).

The Shanul gas reserves are contained beneath the broad, symmetric Shanul anticline, NW of the small settlement of Khalili (Figure 2). This anticline is outlined by resistant carbonates of the Miocene Mishan formation, while its close neighbor to the east — the West Bavush anticline — is expressed in the Oligocene Asmari limestone (Figure 2). A cross-section of the Shanul anticline published by the Geological Survey of Iran (GSI) depicts the Shanul anticline as flanked by steep reverse faults that originate in Paleozoic strata in the anticline core. This view is supported by our own interpretation of newly-available National Iranian Oil Company (NIOC) seismic reflection imagery (Figs. S1, S2). In contrast, the West Bavush anticline has a tighter and more asymmetric (southward divergent) shape, reflecting that its flanking reverse faults originate at shallower (~3 km) depths in Triassic Dashtak evaporites (Figure 2 and Motamedi et al., 2012). The faults underlying both anticlines emerge at the surface as longitudinal reverse faults trending ~N100^o–105^o (Figure 2). A combination of remote-sensing, field, and seismic data permit us to construct a structural cross-section across these anticlines, from surface down to the base of sedimentary cover (Figure 2b).

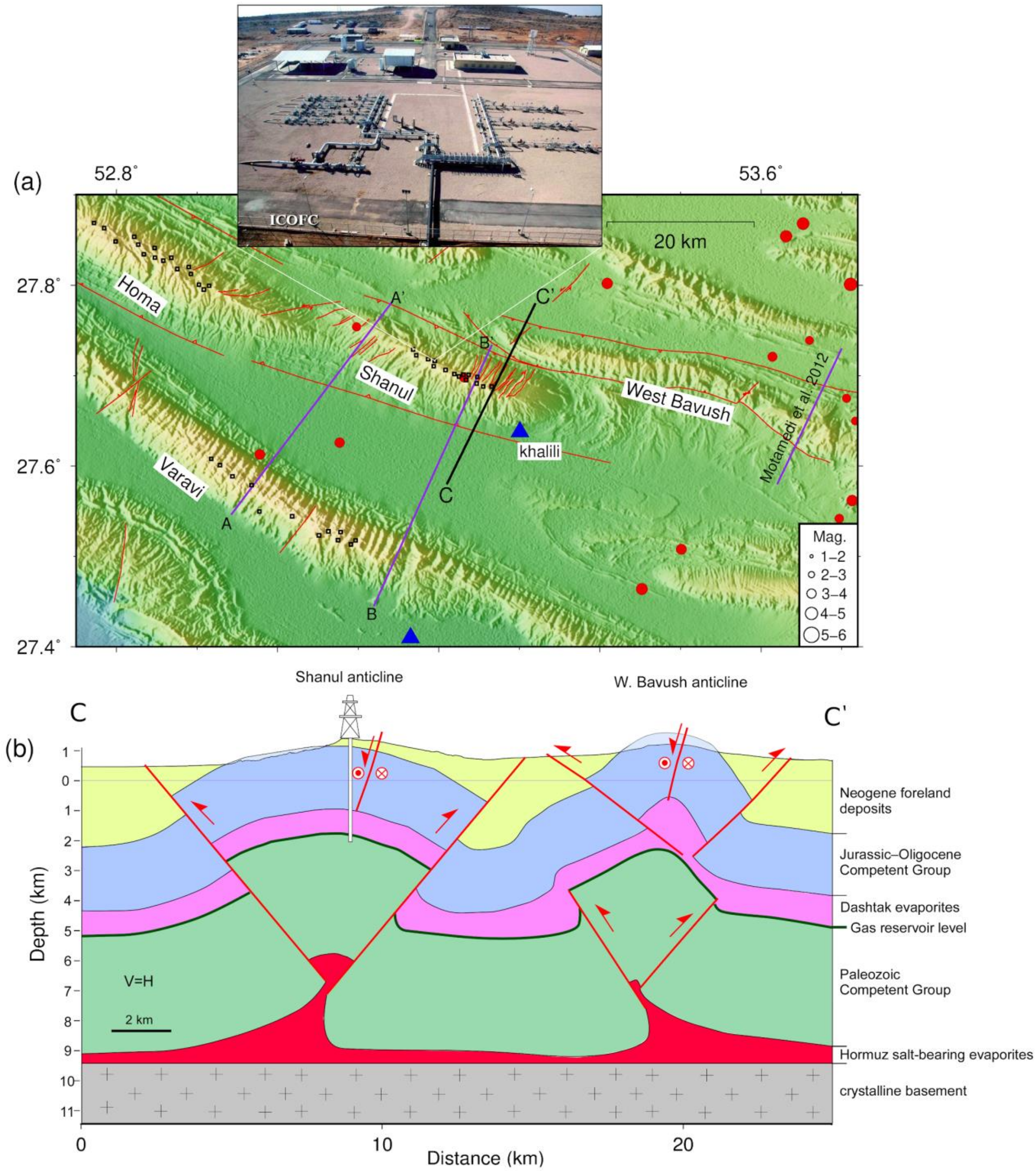

Figure 2. a) Topography, modified map of the faults, background seismicity, the Shanul, and neighboring Homa, Varavi, and West Bavush anticlines. The inset photo shows the Shanul gas field, from ICOFC. Black squares show the location of active wells in the Shanul, Homa, and Varavi gas fields. Red circles are relocated earthquakes before 2019 (Karasözen et al., 2019). Blue triangles show IRSC broadband stations. Purple lines show locations of the seismic profiles (This study and Motamedi et al., 2012). The A–A' and B–B' seismic sections presented in Figs S1 and S2. **b)** The structural cross-section across the Shanul and West Bavush anticlines (C-C' profile), constructed based on an integration of seismic, field and remote-sensing data.

The Shanul reservoir was discovered in 1995 and the first well drilled in 2004, with gas extraction starting in 2006 from Permo-Triassic Dehram Group carbonates, capped by Dashtak evaporites at depth of ~3-4 km (Motamedi et al., 2012; Esrafili-Dizaji & Rahimpour-Bonab, 2013). The gas field belongs to the Iranian Central Oil Fields Company (ICOFC), one of the five major production companies of the NIOC, while the Southern Zagros Oil and Gas Production Company is responsible for its operation, extraction, and injection. So far, 18 wells have been drilled in the Shanul gas field (Figure 2). According to the ICOFC, 35 million cubic meters per day of gas are extracted from the Shanul field and the neighboring Homa reservoir, which together have a capacity of 220 billion cubic meters. Gas extraction from the 16th well of the Shanul field commenced in 2016, producing 600,000 cubic meters per day. Considering the gas capacity and extraction rate, gas reserves from both reservoirs are likely to become depleted within about 3 years. Fluid injection, which is typically applied in the gas fields of Iran when production is waning, is therefore likely to have started in both reservoirs.

There are no historical records of any earthquake unambiguously linked to faults within our study area (Ambraseys and Melville, 1982; Berberian, 1995). Modern seismicity in Iran is monitored and reported by permanent networks of the IRSC and the International Institute of Earthquake Engineering and Seismology (IIEES), which have been densified with time. Relative sparse seismic coverage in the Zagros prior to about 2012 limited the routine detection threshold and location accuracy for small-to-moderate magnitude earthquakes. Nevertheless, the relocated catalog of Karasözen et al. (2019) indicates two events of m_b 4 (on 10 August 2009 and 1 October 2010) that are colocated with the Shanul anticline (Figure 2).

3 Source characteristics of the 2019-2020 Khalili seismic sequence

3.1. Multiple-event relocation

Here we assess the overall spatio-temporal evolution of the 2019–2020 sequence using a multiple-event epicentral relocation. We used the *Mloc* implementation (Bergman & Solomon, 1990) of the hypocentral decomposition algorithm (Jordan and Sverdrup, 1981), consistent with several earlier regional studies (Nissen et al., 2010, 2019; Roustaei et al., 2010; Elliott et al., 2015; Karasözen et al., 2019). IRSC station coverage is sufficient (Figure S3) that we could employ a "direct calibration" (Karasözen et al., 2019) of the 2019-2020 sequence, yielding epicentral uncertainties of less than ~3 km for most of the selected events (Figure S4). Among the ~300 events ($M_n \geq 2.5$) reported by IRSC, we relocated 115 events ($M_n \geq 3.0$) with sufficient numbers of phase readings within epicentral distance of less than 1.8 degree and moderate azimuthal gaps. We use a slightly modified version of the 1-D layered velocity model (Figure S5) of Karasözen et al. (2019) to predict theoretical travel times (Figure S6) at local and regional distances. Owing to insufficient closeby station coverage, we were unable to solve for focal depths of most events. Among the 115 events, the focal depth of 19 events was constrained with phase reading from a very nearby station, but for 96 events the focal depths were fixed to 7 km (Table S3). Therefore the relocated seismicity cannot be used to infer the dip of the causative faulting at depth. From experience, the errors of the assumed focal depth of less than ~15 km have a negligible effect on epicenter accuracy (Ghods et al., 2012).

The spatio-temporal evolution of seismicity clearly depicts two phases of the sequence (Figure 3). Phase 1 started in January 2019 and continued through early 2020, and is swarm-like, lacking a dominant mainshock or clear taper of aftershocks. Phase 1 events follow a WNW–ESE-oriented trend centered on the southern limb of the Shanul anticline. Phase 2 commenced with the M_w 4.7 foreshock on May 31, 2020, and includes the June 9, 2020 M_w 5.4 and 5.7 earthquakes and their aftershocks. Phase 2 seismicity lies along a separate WNW–ESE-oriented trend located between the Shanul and West Bavush anticlines (Figure 3).

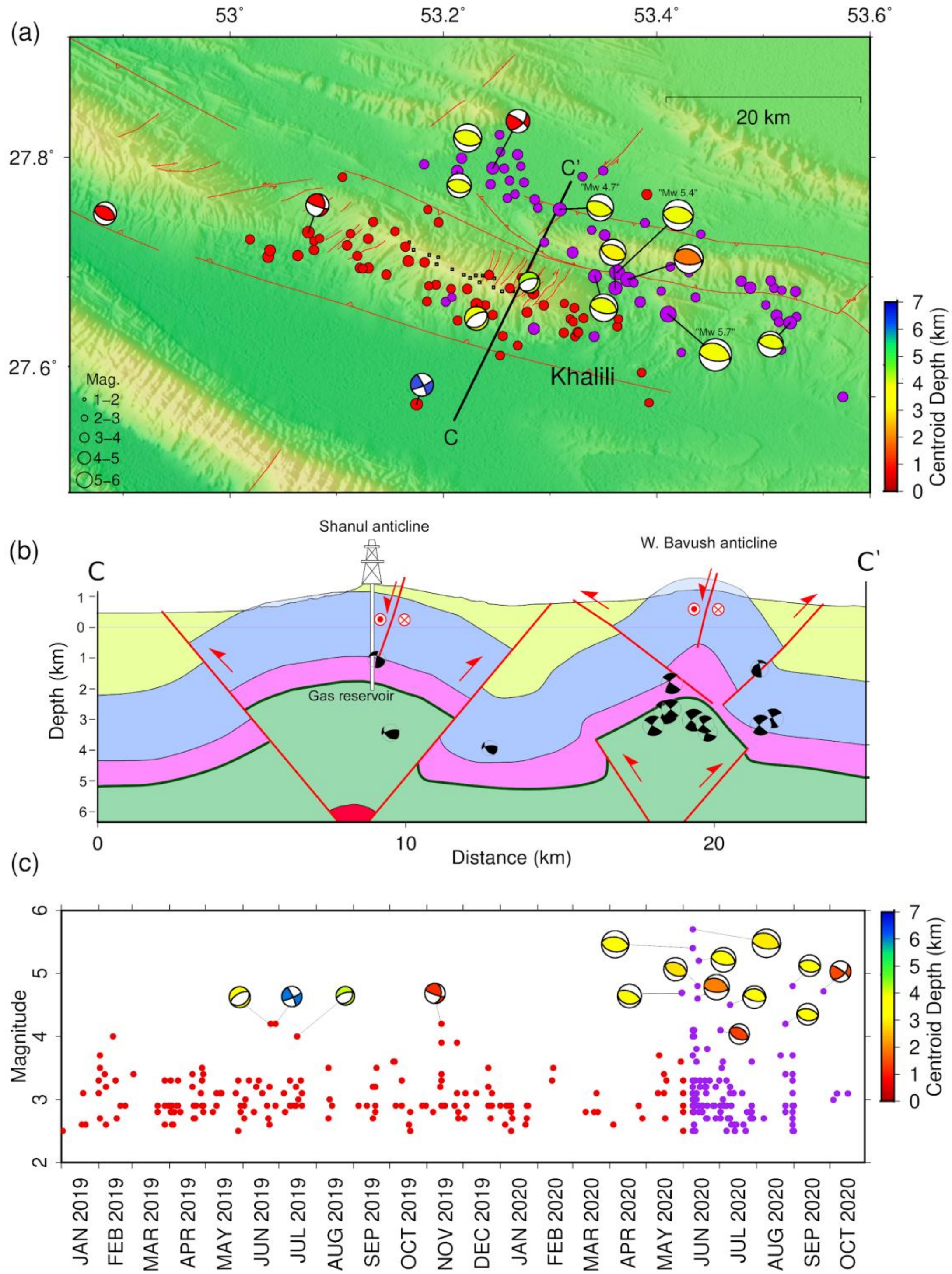

Figure 3. (a) Relocated epicenters of $M_n \geq 3.0$ events and focal mechanisms of $M_n \geq 4.0$ events from January 2019 to October 2020 that are coloured by centroid depth. Red circles are events in phase 1 (prior to May 31, 2020) and purple circles are those in phase 2. Red lines show modified faults in the region (after the GSI) and black squares show the location of active wells in the Shanul gas field. **(b)** The structural cross-section across the Shanul and West Bavush anticlines (C–C' profile, and color same as the Figure 2) and our relocated focal mechanisms at their centroid depths. **(c)** Temporal evolution of seismicity from IRSC catalog ($M_n \geq 2.5$), with events plotted by the magnitude and coloured as in (a).

3.2. Focal depth of the June 9, 2020 M_w 5.7 mainshock

Well-constrained focal depths are an important potential discriminator of induced earthquakes. We use independent, teleseismic data to estimate the focal depth of the June 9, 2020 M_w 5.7 Khalili mainshock.

We modelled the delay between the direct *P* arrival and the surface reflected *pP* phases at teleseismic distances, which depends on the source depth and the average *P* wave velocity above the hypocenter. For this analysis, we used the Array Beam Depth Tool (see *Code Availability*; e.g. Negi et al., 2017). To improve the signal-to-noise ratio, we used array recordings, so that similar waveforms can be stacked to form a beam. For this analysis, we processed independently four different seismic arrays (Figure S7). Observed beams are compared to synthetic ones, computed for different source depths using source and receiver crustal models plus a global mantle model. Results from all four arrays are consistent with a focal depth of ~7 km for the M_w 5.7 earthquake (Figure 4).

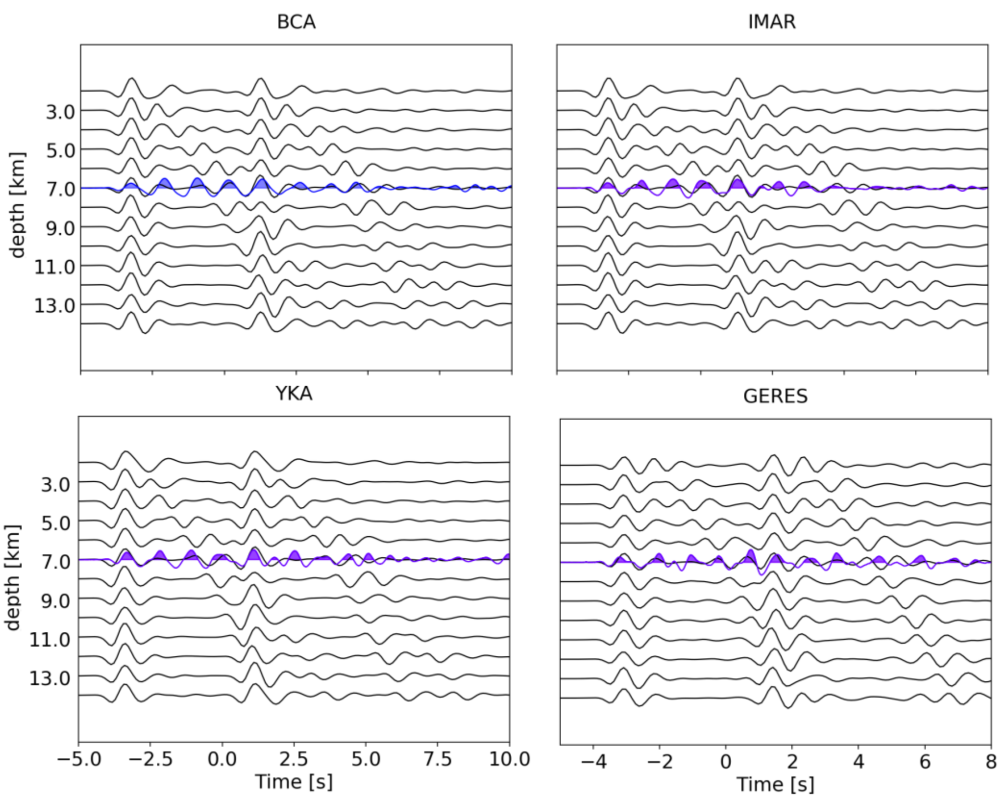

Figure 4. Estimation of the focal depth of the June 9, 2020 M_w 5.7 Khalili mainshock using teleseismic records in four seismic arrays; BCA, IMAR, YKA, and GERES (See the location of arrays in Figure S7). Black lines show synthetic waveforms including depth phases (*P and pP)* based on velocity model and source mechanism in different depths. Blue waveforms represent observed stacked array beams corresponding to each array. A focal depth of 7 km offers the best visual coherency between observed and synthetic traces.

3.3. Regional moment tensor solutions

Full moment tensor (MT) solutions obtained through regional waveform inversions are a key tool for induced seismicity studies, providing critical information on the source geometry and the rupture process (e.g. Dahm et al., 2015). Observations of relevant non-double couple (non-DC) components through MT decomposition have been used as an indicator for a certain type of induced seismicity (e.g. Cesca et al., 2013a; Zhang et al., 2016). For very specific earthquakes, e.g. those involving an underground collapse, a full MT inversion can be directly used to detect specific induced events (e.g. Cesca et al., 2013a). However, most induced earthquakes are characterized by shear fracturing, and full MT inversions and decomposition results are useful more for the inference of the rupture geometry than for discrimination. Furthermore, full MT inversions are challenging for small to moderate magnitude events, requiring a robust assessment of any resulting non double-couple (DC) source terms. Probabilistic waveform inversion techniques, which provide estimations of the parameter uncertainties and trade-offs, provide the best approach to assess reliable non-DC components (Zahradnik et al., 2008; Kühn et al., 2020). Among the parameters which are estimated by a centroid full MT inversion (scalar moment, centroid depth, fault plane angles, and percentages of decomposed MT terms), the centroid depth is particularly important discriminator between anthropogenic and natural seismicity in the region where both are probable (Dahm et al., 2013; Grigoli et al., 2017).

We performed full MT inversions for the four earthquakes in the Khalili sequence; the M_w 5.4 and 5.7 phase 2 events on June 9, 2020 and two events with normal mechanisms in phase 1. We also undertook deviatoric MT inversion — using the standard decomposition between compensated linear vector dipole (CLVD) and double couple terms — for eleven moderate events of M_w 4.0–4.8, including two phase 1 events and seven additional phase 2 events. We used a probabilistic MT inversion method (Heimann et al., 2018), which provides ensembles of best-fitting MTs, which are used to estimate uncertainties and trade-offs for all inverted source parameters. This technique has been successfully applied to other earthquakes in the Zagros, as well as in other regions (e.g. Kühn et al., 2020).

We set up the MT inversion to simultaneously fit 3-components waveforms in the time (full displacement waveforms) and in the frequency domains (full amplitude spectra). Synthetic seismograms were computed using pre-calculated Green's functions (Heimann et al., 2019), based on a velocity model by Karasözen et al., (2019). For events smaller than M_w 5 we adopted the frequency band of 0.02–0.07 Hz; for the larger pair of events, we used the frequency band 0.015–0.05 Hz. To avoid systematic error in the MT solutions due to sensor misorientation, we applied the sensor orientation corrections (Braunmiller et al., 2020) for the IRSC stations. The resolved focal mechanisms are in good agreement with GCMT and GEOFON solutions, for the few cases when they are available, but we estimate in most cases shallower centroid depths, mostly ≤ 4 km with estimated uncertainties of 0.5 km (note that Global CMT has no resolution for shallow depths below 15 km). All obtained source parameters together with their uncertainties (68% confidence intervals) are listed in Table 1.

We observe distinct patterns of focal mechanism in the two phases of the 2019-2020 seismic sequence (Figure 3a). Phase 1 events exhibit diverse mechanisms and depths, comprising one very shallow (1 km centroid depth) reverse faulting event, two normal faulting events at 3-4 km, and a slightly deeper (7 km) strike-slip earthquake. The normal faulting events appear linked to a series of short, shallow, ~NE-trending faults mapped along the crest of the Shanul anticline (Figs. 2, 3), likely the consequence of bending stresses within the upper layer of the fold. Figure S8 shows waveform and amplitude spectra fits for the June 24, 2019 M_w 4.2 event with normal mechanism. We observe that for the pair of normal mechanisms, the non-DC part is larger than the DC part (Figs. S9, S10).

Phase 2 seismicity rather follows a typical foreshock-mainshock-aftershock pattern, with similar ENE–WSW-oriented thrust faulting mechanisms and consistently shallow (≤ 4 km) centroid depths, suggesting rupture occur along a single fault or fault zone, parallel to both the local fold axes and the overall seismicity trend. Figure 5 shows waveform and amplitude spectra fits for the

June 9, 2020 M_w 5.7 mainshock. Our full moment tensor decomposition into isotropic (ISO) and CLVD and DC components reveals a relatively large CLVD component, similar to that resolved independently by GCMT and GEOFON. The M_w 5.7 mainshock centroid depth is shallower (3±1 km) than the focal depth (~7 km, resolved by teleseismic *pP-P* delays in Section 3.2), consistent with upward rupture directivity. In any case, both results point to a shallow source, within the middle-to-upper sedimentary cover.

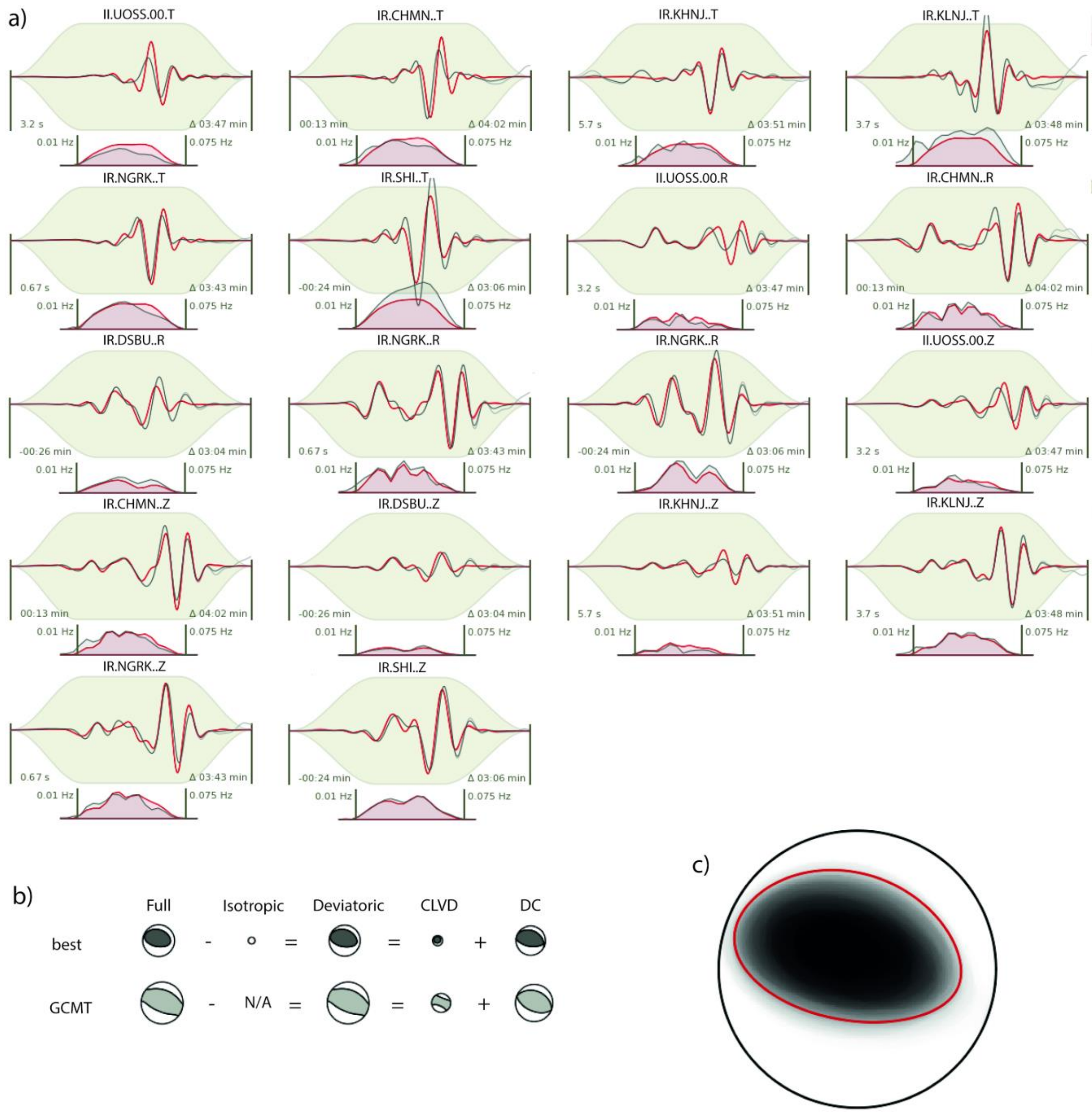

Figure 5. Full moment tensor solution of the June 9, 2020 M_w 5.7 earthquake. **(a)** Waveform fits in time domain and amplitude spectra for the M_w 5.7 earthquake. Red and gray waveforms/spectra show synthetic and observed records, respectively. Information on the top of the waveforms fit gives station names with transverse (T), radial (R) or vertical (Z) components. Numbers within the panels describe the time window and the frequency band **(b)** The decomposition of the full moment tensor in ISO, CLVD, and DC parts. The symbol size indicates the relative strength of the components. The Global Centroid Moment Tensor (GCMT) solution is shown for comparison. **(c)** The fuzzy full MT solution illustrating the uncertainty of the solution.

Table 1. Moment tensor solutions of the 15 events in 2019-2010 Khalili seismic sequence obtained in this study. Table columns refer to the event number, date and time in UTC (yyyy-mm-dd hh:mm:ss), relocated latitude and longitude, Magnitude (M_w), centroid depth, and strikes, dips, and rakes of the two nodal planes with estimated uncertainties.

No	Date and time (UTC)	Latitude°	Longitude°	M_w	Depth (km)	Strike1°	Dip1°	Rake1°	Strike2°	Dip2°	Rake2°
1	2019-06-24 15:14:08	27.677	53.231	4.2	4.0 ± 1.0	244 ± 13	62 ± 3	-85 ± 16	53 ± 14	28 ± 5	-99 ± 20
2	2019-06-28 09:08:54	27.594	53.175	4.2	6.0 ± 1.0	335 ± 24	83 ± 2	170 ± 46	66 ± 2	80 ± 2	7 ± 2
3	2019-07-16 12:02:24	27.686	53.284	4.0	4.0 ± 2.0	265 ± 56	64 ± 7	-56 ± 25	28 ± 14	41 ± 12	-138 ± 42
4	2019-11-13 17:57:45	27.737	53.073	4.2	1.0 ± 0.5	6 ± 20	37 ± 5	163 ± 4	110 ± 5	80 ± 3	53 ± 4
5	2020-05-31 23:59:00	27.756	53.309	4.7	3.0 ± 0.5	292 ± 5	58 ± 4	99 ± 5	96 ± 5	33 ± 3	76 ± 8
6	2020-06-09 16:08:48	27.704	53.363	5.4	3.0 ± 0.5	278 ± 5	46 ± 3	90 ± 8	98 ± 6	44 ± 3	90 ± 7
7	2020-06-09 17:18:12	27.669	53.411	5.7	3.0 ± 1.0	97 ± 7	58 ± 6	79 ± 8	297 ± 8	33 ± 6	107 ± 12
8	2020-06-13 22:04:14	27.691	53.361	4.8	3.0 ± 0.5	294 ± 4	33 ± 2	100 ± 6	102 ± 4	57 ± 1	83 ± 4
9	2020-06-13 23:15:03	27.701	53.342	4.6	3.0 ± 0.5	288 ± 9	43 ± 6	85 ± 13	115 ± 9	47 ± 6	95 ± 12
10	2020-06-14 18:06:00	27.698	53.373	5.2	2.0 ± 0.5	296 ± 10	35 ± 11	110 ± 14	92 ± 11	57 ± 10	77 ± 15
11	2020-07-02 00:29:00	27.739	52.885	4.1	1.0 ± 0.5	304 ± 6	43 ± 10	100 ± 9	112 ± 8	48=11	82 ± 8
12	2020-07-10 20:14:04	27.662	53.525	4.5	4.0 ± 0.5	276 ± 5	26 ± 2	83 ± 8	104 ± 4	64 ± 2	93 ± 4
13	2020-08-25 12:16:00	27.788	53.213	4.2	3.5 ± 0.5	280 ± 6	48 ± 4	90 ± 7	100 ± 6	41 ± 4	90 ± 8
14	2020-08-31 03:36:50	27.810	53.222	4.8	3.0 ± 0.5	284 ± 3	45 ± 2	91 ± 2	103 ± 3	45 ± 2	89 ± 3
15	2020-09-08 01:34:17	27.791	53.246	4.3	1.5 ± 0.5	305 ± 9	77 ± 11	144 ± 21	44 ± 20	55 ± 11	15 ± 21

3.4. Fault geometry and slip distribution of the June 9, 2020 M_w 5.7 earthquake from InSAR modeling

We used Sentinel-1 InSAR imagery and elastic dislocation modelling to characterize the June 9, 2020 M_w 5.7 mainshock fault geometry and coseismic slip distribution. Using the earliest available post-seismic acquisitions, we constructed one twelve-day interferogram on descending-track D64, and two twenty-four-day interferograms on ascending tracks A130 and A28 (Figure 6a). The interferograms also each capture the M_w 5.4 foreshock that occurred 70 minutes before the mainshock. All three interferograms exhibit a WNW–ESE-oriented pattern of deformation, containing 3–4 fringes, equivalent to ~10 cm of displacement towards the satellite. The close similarity of fringe patterns in the descending- and ascending-track interferograms implies that this deformation is predominantly uplift, centered upon a tight syncline between the Shanul and West Bavush anticlines. A single fringe (~3 cm) of deformation away from the satellite is also evident to the North of the main fringe ellipse, colocated with the northern limb of the West Bavush anticline.

To characterize the fault geometry and slip distribution responsible for the observed fringe patterns, we followed routine elastic dislocation modelling procedures (Okada, 1985; Wright et al., 1999; Funning et al., 2005) that have been applied to other earthquake sequences in the Fars arc (e.g. Nissen et al., 2010; Roustaei et al., 2010; Elliott et al., 2015). Full details are provided in Supplementary text S1. We found that both NNE- and SSW-dipping model faults could reproduce the overall InSAR deformation pattern, but that in either case, a kinked, two-fault geometry offered noticeable visual and numerical improvements over a single slip plane. Based on the adjacency of the mainshock hypocentral locations, as well as the narrow aftershock cloud, our preferred configuration is the SSW-dipping, two-fault model (Figure 6 a,b), though alternative models are also provided in Supplementary file (Figs. S11–S15).

The preferred model faulting parallels the West Bavush anticline but projects to the surface close to its axial trace, and is thus offset southwards from the SSW-dipping fault interpreted in Figure 3b. The ~15 km-long western InSAR model fault segment strikes 108°, dips 64° N, and has a rake of 84°; the shorter ~5 km-long eastern model fault segment strikes 95°, dips 66° N and has a rake of 110°. Near the mainshock hypocenter, slip is concentrated at depths of ~2–8 km, but elsewhere it falls within an even narrower range of ~2–6 km (Figure 6b), consistent with the 3±1 km centroid depth resolved using seismological data. The hypocenter is located close to the bottom of the slip patch and at about midway along its length, indicating rupture propagation up-dip and bilaterally along strike. The upward directivity may be responsible for the extensive damage in the hanging wall of the mainshock fault, and could help explain the widespread occurrence of land sliding evident in satellite photographs (Valkaniotis, 2020).

The InSAR model moment of ~6.6 $\times 10^{17}$Nm (M_w 5.8) is roughly 50% larger that of the mainshock GCMT and USGS W-phase solutions (4.2–4.3 $\times 10^{17}$Nm, M_w 5.7). The M_w 5.4 foreshock can account for much of the difference, though it is possible that our models also include a small amount of postseismic afterslip.

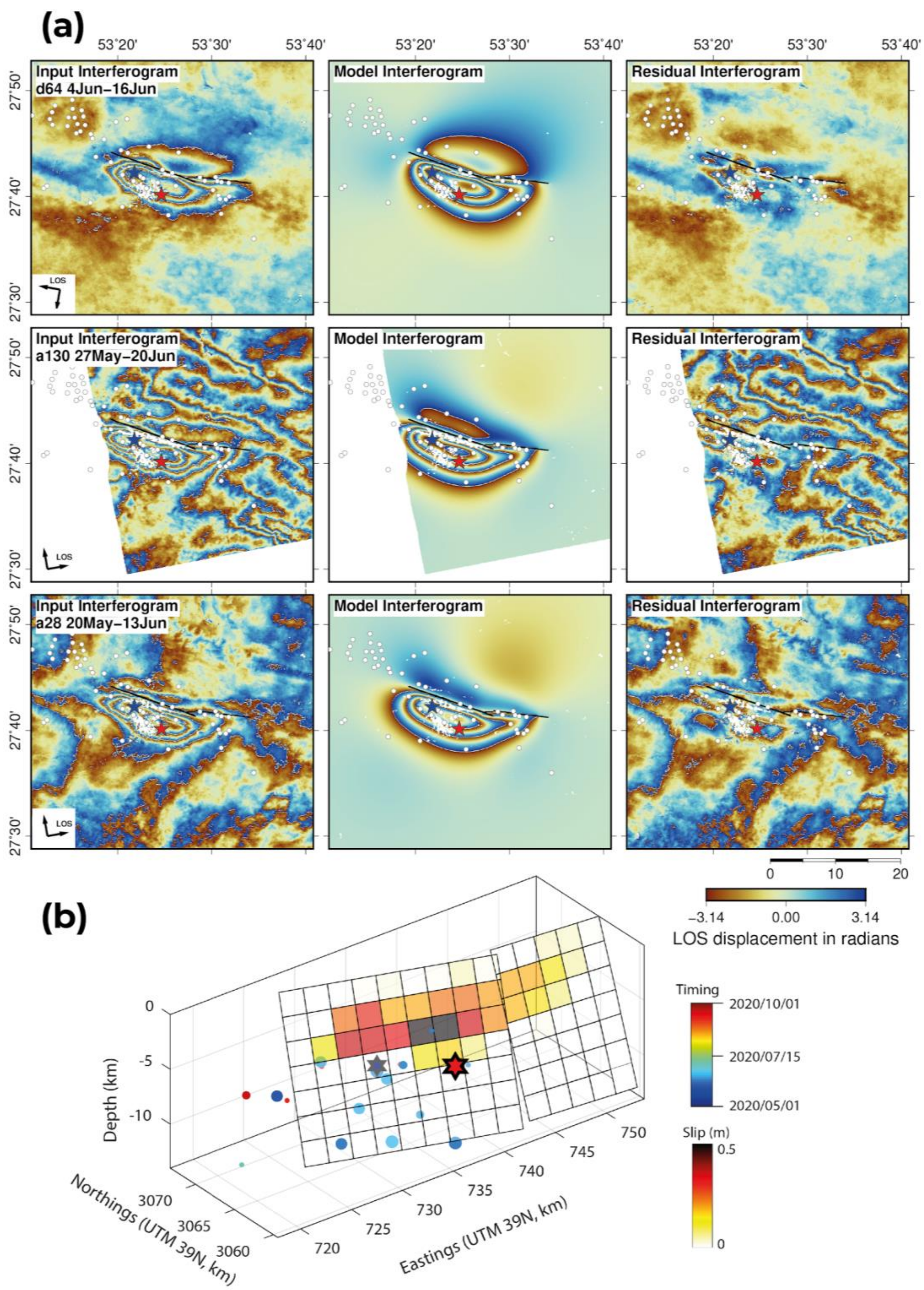

Figure 6. (a) From top to bottom: coseismic interferograms on tracks D64, A130, and A28. From left to right: observed, model, and residual interferograms. Results are shown rewrapped in order to accentuate deformation gradients (2π radians = 2.77 cm displacement). The black line is the surface projection of the model faults. Red and blue stars are relocated epicenters of the M_w 5.7 and M_w 5.4 earthquakes, respectively, and white dots are relocated aftershocks (phase 2). **(b)** Coseismic slip distribution from modeling the InSAR data. The model fault is divided into

2 km square patches. Red and grey stars are hypocenters of the M_w 5.7 and M_w 5.4 earthquakes, respectively. Circles show the relocated 20 aftershocks, which the focal depths of them were constrained with phase reading from a very nearby station, and coloured according to time.

4 Discussion: was the 2019–2020 Khalili sequence induced?

Observations that unequivocally link a seismic sequence to fluid injection time-series in a gas field are rare. Here, we have no access to the kinds of production data — such as extraction/injection time-series, volumes, and pressures of the injected fluid — that could confirm a causative link to trends in the temporal evolution of seismicity. However, the timing of the 2019-2020 Khalili sequence is at least consistent with an anthropogenic origin. The first well in the Shanul gas field was drilled in 2004, and gas extraction started in 2006. However, fluid injection started later, only after production had peaked. Seismicity in the Shanul gas field emerged several years after the start of extraction. Time delays of several months or even several years between the start of production and the emergence of induced seismicity have been observed in other gas fields. For example, in the Groningen region of the Netherlands the first earthquake occurred after 28 years of production (Richter et al., 2020), while earthquake sequences near the Oklahoma Wilzetta and Texas Cogdell oil fields commenced ~20 years after the initiation of fluid injection (Keranen et al., 2014).

We can also compare source characteristics of the 2019-2020 Khalili sequence with those of natural, background seismicity in the Fars arc. Our calibrated relocation of the seismic sequence reveals two distinct clusters in space and time. The first phase is spatially localized in the southern part of the Shanul gas reservoir and resembles a swarm without a clear mainshock (Figure 3c). Three out of four centroid depths (1– 4 km) are close to the probable production levels of the reservoir (~3-4 km), and differ markedly from the ~10-20 km depths typical of small-to-moderate earthquakes in neighboring parts of the Zagros (e.g. Tatar et al., 2004; Nissen et al., 2011). This phase also exhibits a wide variety of mechanisms, including two normal faulting events with significant non-DC components. We interpret that the first phase was induced by fluid injection in the Shanul gas reservoir. Pore pressure changes can induce or trigger slip on pre-existing faults (such as those identified in regional geological maps and seismic lines), and can explain the phase 1.

The second phase of the sequence commenced with the M_w 4.7 foreshock on May 31, 2020, and culminated in the M_w 5.4 and 5.7 earthquakes on June 9. This phase is centered upon the West Bavush anticline, ~15 km NE of the Shanul reservoir. Similar to the first phase, it is marked by shallow centroid depths of ≤ 4 km. However, unlike the first phase, the second phase exhibits typical foreshock-mainshock-aftershock patterns and reverse faulting mechanisms that are compatible with regional tectonic stresses. The June 9, 2020 M_w 5.7 mainshock ruptured a steep, SSW-dipping reverse fault within the core of the west Bavush anticline, nucleating at 7 km depth but releasing most of its moment at shallower depths of ~2–6 km, within the upper half of the sedimentary cover. The fault width (~4 km) is thus narrow with respect to the fault length (~20 km), similar to patterns observed elsewhere in the Fars arc and presumably reflecting lithologic barriers to up- and down-dip rupture propagation (Roustaei et al., 2010; Elliott et al., 2015).

Most well-recorded Fars arc earthquakes of similar magnitude to the Khalili mainshock — such as those at Qeshm Island in 2005–2008, Fin in 2006, and Khaki-Shonbe in 2013 — were centered in the middle or lower cover (at depths of ~5–9 km), and their aftershock sequences included concentrations of events at unequivocal basement depths (Nissen et al., 2010, 2014;

Lohman & Barnhart 2010; Roustaei et al., 2010; Elliott et al., 2015). The shallow depths of phase 2 of the Khalili sequence are therefore unusual, but they are not unprecedented. The 2013 M_w 6.2 Khaki-Shonbe earthquake ruptured a subsidiary fault plane (southeast of the deeper, main rupture) at shallow depths of ~2–4 km (Elliott et al., 2015), and the nearby 2014 M_w 5.1 Bushkan earthquake slipped at depths of ~2–6 km (Kintner et al., 2019). We note that both these shallow slip planes are associated with anticlinal structures containing active gas fields (Khaki-Shonbe earthquake; the Kangan and Zireh fields and Bushkan earthquake; the Dalan field), though further study would be needed to assess whether they might also have been induced.

The depths of phase 2 events are also similar to those reported for induced seismicity associated with hydrocarbon reservoirs in other regions (e.g. Cesca et al., 2014; Dahm et al., 2015). We therefore interpret that while the second phase involved the release of background tectonic stresses, it was likely triggered by stress changes from the first stage or fluid migration, by means of pore pressure diffusion or poroelastic stresses. Fluid migration may reach large distances of tens of kilometers (e.g. Goebel et al., 2017), which makes this hypothesis fully compatible with the location of phase 2 events, and can occur over relatively long time periods. The timing of such a triggering process cannot be accurately discussed here, due to the lack of knowledge on local diffusivity conditions and the potential presence of pathways controlling fluid migration, but a delay of 4-5 months between phase 1 and 2 at ~10 km distances appears to be compatible with previous observations of fluid-driven seismicity (e.g. Hainzl et al., 2012).

The lack of subsurface fluid flow data and or constraints on geomechanical properties preclude us from quantifying the likelihood of induced or triggered seismicity through physics-based probabilistic modeling (Dahm et al., 2015). However, as a check on our interpretation of the

2019–2020 Khalili sequence as being of anthropogenic origin, we applied qualitative discrimination approaches based on a series of questions. Application of the Frohlich et al. (2016a) criteria support our inference that the Khalili earthquake sequence is induced. Moreover, we applied a new framework proposed by Verdon et al., (2019), comprising a series of variably weighted questions with positive numerical scores assigned to characteristics of induced seismicity (+100%) and negative scores to those of natural events (-100%). Our seismological analysis allows us to obtain an induced assessment ratio (IAR) of +40% with a high evidence strength ratio (ESR) of 94.8% (ranging between 0 to 100%) supporting the quality and quantity of information used in the assessment (Figs. S16, S17). Results strongly support our inference that the 2019–2020 Khalili seismic sequence was induced.

5 Conclusions

We present a detailed analysis of the 2019-2020 Khalili seismic sequence in the Fars arc of Zagros Simply Folded Belt. The proximity of this sequence to the Shanul gas field, from which a very large volume of gas has been extracted over ~14 years, raised the possibility that these were induced events. We analysed the sequence using local, regional and teleseismic data, and further constrained the largest earthquake with InSAR modeling. A comparison with previous background seismicity highlights the anomalously shallow depths of the 2019–2020 sequence, suggesting human-induced stress changes related to operation in the Shanul gas field caused the Khalili seismic sequence. This inference is further supported by the application of a variety of qualitative indicators, but a more sophisticated, probabilistic assessment would require injection/extraction data, which are lacking. This is, to our knowledge, the first case of anthropogenic seismicity directly linked to gas extraction in the Zagros. Triggering of the M_w 5.4

and 5.7 events highlights the need to identify large faults in the vicinity of active gas fields, and to avoid pore-pressure perturbations that could destabilize these faults. Iran already hosts a significant number of proven hydrocarbon reservoirs and has huge potential for new discoveries. For instance, in 2019, the NIOC discovered a gas reservoir ~20 km north of the Shanul field, named Eram, with a very considerable gas capacity. Our results suggest that the exploitation of these reservoirs should be preceded by risk assessment studies and accompanied by the implementation of dedicated, sophisticated monitoring, which would allow the seismic activity to be detected early and its evolution tracked.

Acknowledgment

This work was supported by the International Training Course "Seismology and Seismic Hazard Assessment" which has been funded by the GeoForschungsZentrum Potsdam (GFZ) and the German Federal Foreign Office through the German Humanitarian Assistance program, grant S08-60 321.50 ALL 03/19. Furthermore, M.J. acknowledges support by a grant from the Iran National Science Foundation (INSF) under a research project number “97013349”. E.N. was supported by the Natural Sciences and Engineering Research Council of Canada through Discovery Grant 2017-04029, the Canada Foundation for Innovation, the British Columbia Knowledge Development Fund, and a Tier 2 Canada Research Chair. J.A. L.-C. has also received funding from the European Union’s Horizon 2020 research and innovation program under the Marie Skłodowska-Curie grant agreement No. 754446 and UGR Research and Knowledge Transfer Found–Athenea3i; and by project 407141557 of the Deutsche Forschungsgemeinschaft (DFG, German Research Foundation).
Maps were prepared using the Pyrocko toolbox and GMT 5 software. We are grateful to all data research centers and networks for providing the data used in this study. InSAR interferograms were made using freely available Copernicus Sentinel data (2017; https://scihub.copernicus.eu/).
We are thankful to Gudrun Richter, Christian Heberland, Sebastian Hainzl, Torsten Dahm and Mir Ali Hassanzadeh for constructive comments on this work.

Data availability

The seismic catalog and waveforms of the Iran network were downloaded from the Iranian Seismological Center available at http://irsc.ut.ac.ir/. Regional and teleseismic broadband seismograms were downloaded from the Incorporated Research Institutions for Seismology (IRIS) Data Management Center. InSAR interferograms were made using Copernicus Sentinel data available at https://scihub.copernicus.eu/. Information on the Shanul and Homa gas reservoirs obtained from the Iranian Central Oil Fields Company webpage (ICOFC, https://en.icofc.ir/), Southern Zagros Oil and Gas Production Company (https://www.szogpc.com/), and National Iranian Oil Company (NIOC). The geological map of the region, which is published by the Geological Survey of Iran (GSI), available at https://gsi.ir/en.

Code Availability

Some of the maps were prepared using the Pyrocko toolbox (https://pyrocko.org/), and GMT 5 software (https://www.generic-mapping-tools.org/). For relocation, we used the mloc program (https://seismo.com/mloc/). The probabilistic source inversion was performed with the Grond framework (Heimann et al., 2018). InSAR data were processed using GAMMA software (https://www.gamma-rs.ch/) and downsampled and inverted using codes developed by the Centre for the Observation and Modelling of Earthquakes, Volcanoes and Tectonics (COMET) group (https://comet.nerc.ac.uk/), available from the E.N. upon request. The mainshock focal depth was calculated using 'Abedeto' tools (https://github.com/HerrMuellerluedenscheid/ArrayBeamDepthTool).

References

Allen, M. B., Saville, C., Blanc, E. J.-P., Talebian, M., & Nissen, E. (2013). Orogenic plateau growth: Expansion of the Turkish-Iranian Plateau across the Zagros fold-and-thrust belt. *Tectonics*, *32*(2), 171–190. https://doi.org/10.1002/tect.20025

Ambraseys, N. N., & Melville, C. P. (1982). A history of Persian earthquakes. Cambridge: Cambridge University Press.

Barnhart, W. D., & Lohman, R. B. (2012). Regional trends in active diapirism revealed by mountain range-scale InSAR time series. *Geophysical Research Letters*, 39(8). https://doi.org/10.1029/2012GL051255

Barnhart, W. D., Lohman, R. B., & Mellors, R. J. (2013). Active accommodation of plate convergence in Southern Iran: Earthquake locations, triggered aseismic slip, and regional strain rates. Journal of Geophysical Research: Solid Earth, 118(10), 5699–5711. https://doi.org/10.1002/jgrb.50380

Berberian, M. (1995). Master "blind" thrust faults hidden under the Zagros folds: Active basement tectonics and surface morphotectonics. *Tectonophysics*, *241*(3), 193–224. https://doi.org/10.1016/0040-1951(94)00185-C

Bergman, E. A., & Solomon, S. C. (1990). Earthquake swarms on the Mid-Atlantic Ridge: Products of magmatism or extensional tectonics? *Journal of Geophysical Research: Solid Earth*, *95*(B4), 4943–4965. https://doi.org/10.1029/JB095iB04p04943

Braunmiller, J., Nabelek, J., & Ghods, A. (2020). Sensor Orientation of Iranian Broadband Seismic Stations from P-Wave Particle Motion. *Seismological Research Letters*, *91*(3), 1660–1671. https://doi.org/10.1785/0220200019

Cesca, S., Rohr, A., & Dahm, T. (2013a). Discrimination of induced seismicity by full moment tensor inversion and decomposition. *Journal of Seismology*, *17*(1), 147–163. https://doi.org/10.1007/s10950-012-9305-8

Cesca, S., Grigoli, F., Heimann, S., González, Á., Buforn, E., Maghsoudi, et al. (2014). The 2013 September–October seismic sequence offshore Spain: A case of seismicity triggered by gas injection? *Geophysical Journal International*, *198*(2), 941–953. https://doi.org/10.1093/gji/ggu172

Dahm, T., Becker, D., Bischoff, M., Cesca, S., Dost, B., Fritschen, R., et al. (2013). Recommendation for the discrimination of human-related and natural seismicity. *Journal of Seismology*, *17*(1), 197–202. https://doi.org/10.1007/s10950-012-9295-6

Dahm, T., Cesca, S., Hainzl, S., Braun, T., & Krüger, F. (2015). Discrimination between induced, triggered, and natural earthquakes close to hydrocarbon reservoirs: A probabilistic approach based on the modeling of depletion-induced stress changes and seismological source parameters. *Journal of Geophysical Research: Solid Earth*, *120*(4), 2491–2509. https://doi.org/10.1002/2014JB011778

Edey, A., Allen, M. B., & Nilfouroushan, F. (2020). Kinematic Variation Within the Fars Arc, Eastern Zagros, and the Development of Fold-and-Thrust Belt Curvature. *Tectonics*, *39*(8), e2019TC005941. https://doi.org/10.1029/2019TC005941

Elliott, J. R., Bergman, E. A., Copley, A. C., Ghods, A. R., Nissen, E. K., Oveisi, B., et al. (2015). The 2013 Mw 6.2 Khaki-Shonbe (Iran) Earthquake: Insights into seismic and aseismic shortening of the Zagros sedimentary cover. *Earth and Space Science*, *2*(11), 435–471. https://doi.org/10.1002/2015EA000098

Ellsworth, W. L. (2013). Injection-Induced Earthquakes. *Science*, *341*(6142). https://doi.org/10.1126/science.1225942

Esrafili-Dizaji, B., & Rahimpour-Bonab, H. (2013). A Review of Permo-Triassic Reservoir Rocks in the Zagros Area, Sw Iran: Influence of the Qatar-Fars Arch. *Journal of Petroleum Geology*, *36*(3), 257–279. https://doi.org/10.1111/jpg.12555

Foulger, G. R., Wilson, M. P., Gluyas, J. G., Julian, B. R., & Davies, R. J. (2018). Global review of human-induced earthquakes. *Earth-Science Reviews*, *178*, 438–514. https://doi.org/10.1016/j.earscirev.2017.07.008

Frohlich, C., DeShon, H., Stump, B., Hayward, C., Hornbach, M., & Walter, J. I. (2016). A Historical Review of Induced Earthquakes in Texas. *Seismological Research Letters*, *87*(4), 1022–1038. https://doi.org/10.1785/0220160016

Funning, G. J., Parsons, B., Wright, T. J., Jackson, J. A., & Fielding, E. J. (2005). Surface displacements and source parameters of the 2003 Bam (Iran) earthquake from Envisat advanced synthetic aperture radar imagery. *Journal of Geophysical Research: Solid Earth*, *110*(B9). https://doi.org/10.1029/2004JB003338

Ghods, A., Rezapour, M., Bergman, E., Mortezanejad, G., & Talebian, M. (2012). Relocation of the 2006 Mw 6.1 Silakhour, Iran, Earthquake Sequence: Details of Fault Segmentation on the Main Recent FaultRelocation of the 2006 Mw 6.1 Silakhour, Iran, Earthquake Sequence: Details of Fault Segmentation. *Bulletin of the Seismological Society of America*, *102*(1), 398–416. https://doi.org/10.1785/0120110009

Goebel, T. H. W., Weingarten, M., Chen, X., Haffener, J., & Brodsky, E. E. (2017). The 2016 Mw5.1 Fairview, Oklahoma earthquakes: Evidence for long-range poroelastic triggering at >40 km from fluid disposal wells. *Earth and Planetary Science Letters*, *472*, 50–61. https://doi.org/10.1016/j.epsl.2017.05.011

Grigoli, F., Cesca, S., Priolo, E., Rinaldi, A. P., Clinton, J. F., Stabile, T. A., et al. (2017). Current challenges in monitoring, discrimination, and management of induced seismicity related to underground industrial activities: A European perspective. *Reviews of Geophysics*, *55*(2), 310–340. https://doi.org/10.1002/2016RG000542

Grigoli, F., Cesca, S., Rinaldi, A. P., Manconi, A., López-Comino, J. A., Clinton, J. F., et al. (2018). The November 2017 Mw 5.5 Pohang earthquake: A possible case of induced seismicity in South Korea. *Science*, *360*(6392), 1003–1006. https://doi.org/10.1126/science.aat2010

Hainzl, S., Fischer, T., & Dahm, T. (2012). Seismicity-based estimation of the driving fluid pressure in the case of swarm activity in Western Bohemia. *Geophysical Journal International*, *191*(1), 271–281. https://doi.org/10.1111/j.1365-246X.2012.05610.x

Heimann, S., Isken, M., Kühn, D., Sudhaus, H., Steinberg, A., Daout, S., et al. (2018). *Grond—A probabilistic earthquake source inversion framework* (1.0, p. 32813 Bytes, 5 Files). GFZ Data Services. https://doi.org/10.5880/GFZ.2.1.2018.003

Heimann, S., Vasyura-Bathke, H., Sudhaus, H., Isken, M. P., Kriegerowski, M., Steinberg, A., & Dahm, T. (2019). A Python framework for efficient use of pre-computed Green's functions in seismological and other physical forward and inverse source problems. *Solid Earth*, *10*(6), 1921–1935. https://doi.org/10.5194/se-10-1921-2019

Jahani, S., Callot, J. P., Letouzey, J., & Frizon de Lamotte, D. (2009). The eastern termination of the Zagros Fold-and-Thrust Belt, Iran: Structures, evolution, and relationships between salt plugs, folding, and faulting. *Tectonics*, 28(6). https://doi.org/10.1029/2008TC002418

Jahani, S., Hassanpour, J., Mohammadi-Firouz, S., Letouzey, J., Frizon de Lamotte, D., et al. (2017). Salt tectonics and tear faulting in the central part of the Zagros Fold-Thrust Belt, Iran. *Marine and Petroleum Geology*, *86*, 426–446. https://doi.org/10.1016/j.marpetgeo.2017.06.003

Jordan, T. H., & Sverdrup, K. A. (1981). Teleseismic location techniques and their application to earthquake clusters in the South-Central Pacific. *Bulletin of the Seismological Society of America*, *71*(4), 1105–1130.

Kangi, A., & Heidari, N. (2008). Reservoir-induced seismicity in Karun III dam (Southwestern Iran). *Journal of Seismology*, *12*(4), 519–527. https://doi.org/10.1007/s10950-008-9104-4

Karasözen, E., Nissen, E., Bergman, E. A., & Ghods, A. (2019). Seismotectonics of the Zagros (Iran) From Orogen-Wide, Calibrated Earthquake Relocations. *Journal of Geophysical Research: Solid Earth*, *124*(8), 9109–9129. https://doi.org/10.1029/2019JB017336

Keranen, K. M., & Weingarten, M. (2018). Induced Seismicity. *Annual Review of Earth and Planetary Sciences*, *46*(1), 149–174. https://doi.org/10.1146/annurev-earth-082517-010054

Keranen, K. M., Weingarten, M., Abers, G. A., Bekins, B. A., & Ge, S. (2014). Sharp increase in central Oklahoma seismicity since 2008 induced by massive wastewater injection. *Science*, *345*(6195), 448–451. https://doi.org/10.1126/science.1255802

Kundu, B., Vissa, N. K., Gahalaut, K., Gahalaut, V. K., Panda, D., & Malik, K. (2019). Influence of anthropogenic groundwater pumping on the 2017 November 12 M7.3 Iran–Iraq border earthquake. *Geophysical Journal International*, *218*(2), 833–839. https://doi.org/10.1093/gji/ggz195

Kintner, J. A., Wauthier, C., & Ammon, C. J. (2019). InSAR and seismic analyses of the 2014–15 earthquake sequence near Bushkan, Iran: Shallow faulting in the core of an anticline fold. *Geophysical Journal International*, *217*(2), 1011–1023. https://doi.org/10.1093/gji/ggz065

Kühn, D., Heimann, S., Isken, M. P., Ruigrok, E., & Dost, B. (2020). Probabilistic Moment Tensor Inversion for Hydrocarbon-Induced Seismicity in the Groningen Gas Field, The Netherlands, Part 1: Testing. *Bulletin of the Seismological Society of America*, *110*(5), 2095–2111. https://doi.org/10.1785/0120200099

Lohman, R. B., & Barnhart, W. D. (2010). Evaluation of earthquake triggering during the 2005–2008 earthquake sequence on Qeshm Island, Iran. *Journal of Geophysical Research: Solid Earth*, *115*(B12). https://doi.org/10.1029/2010JB007710

Mansouri-Daneshvar, M. R., Ebrahimi, M., & Nejadsoleymani, H. (2018). Investigation of mining-induced earthquakes in Iran within a time window of 2006–2013. *Journal of Seismology*, *22*(6), 1437–1450. https://doi.org/10.1007/s10950-018-9776-3

Motamedi, H., Sherkati, S., & Sepehr, M. (2012). Structural style variation and its impact on hydrocarbon traps in central Fars, southern Zagros folded belt, Iran. *Journal of Structural Geology*, *37*, 124–133. https://doi.org/10.1016/j.jsg.2012.01.021

Najafi, M., Yassaghi, A., Bahroudi, A., Vergés, J., & Sherkati, S. (2014). Impact of the Late Triassic Dashtak intermediate detachment horizon on anticline geometry in the Central Frontal Fars, SE Zagros fold belt, Iran. *Marine and Petroleum Geology*, *54*, 23–36. https://doi.org/10.1016/j.marpetgeo.2014.02.010

Nissen, E., Yamini-Fard, F., Tatar, M., Gholamzadeh, A., Bergman, E., Elliott, J. R., et al. (2010). The vertical separation of mainshock rupture and microseismicity at Qeshm island in the Zagros fold-and-thrust belt, Iran. *Earth and Planetary Science Letters*, *296*(3), 181–194. https://doi.org/10.1016/j.epsl.2010.04.049

Nissen, E., Tatar, M., Jackson, J. A., & Allen, M. B. (2011). New views on earthquake faulting in the Zagros fold-and-thrust belt of Iran. *Geophysical Journal International*, *186*(3), 928–944. https://doi.org/10.1111/j.1365-246X.2011.05119.x

Nissen, E., Ghods, A., Karasözen, A., Elliott, J. R. Barnhart, W. D. Bergman, E. A., et al. (2019). The 12 November 2017 M w 7.3 Ezgeleh-Sarpolzahab (Iran) earthquake and active tectonics of the Lurestan arc. Journal of Geophysical Research: Solid Earth, 124. https://doi.org/10.1029/2018JB016221

Nissen, E., Jackson, J., Jahani, S., & Tatar, M. (2014). Zagros "phantom earthquakes" reassessed—The interplay of seismicity and deep salt flow in the Simply Folded Belt? *Journal of Geophysical Research: Solid Earth*, *119*(4), 3561–3583. https://doi.org/10.1002/2013JB010796

Negi, S. S., Paul, A., Cesca, S., Kamal, Kriegerowski, M., Mahesh, P., & Gupta, S. (2017). Crustal velocity structure and earthquake processes of Garhwal-Kumaun Himalaya: Constraints from regional waveform inversion and array beam modeling. *Tectonophysics*, *712–713*, 45–63. https://doi.org/10.1016/j.tecto.2017.05.007

Okada, Y. (1985). Surface deformation due to shear and tensile faults in a half-space. *Bulletin of the Seismological Society of America*, *75*(4), 1135–1154.

Richter, G., Hainzl, S., Dahm, T., & Zöller, G. (2020). Stress-based, statistical modeling of the induced seismicity at the Groningen gas field, The Netherlands. *Environmental Earth Sciences*, *79*(11), 252. https://doi.org/10.1007/s12665-020-08941-4

Roustaei, M., Nissen, E., Abbassi, M., Gholamzadeh, A., Ghorashi, M., Tatar, M., et al. (2010). The 2006 March 25 Fin earthquakes (Iran)—Insights into the vertical extents of faulting in the Zagros Simply Folded Belt. *Geophysical Journal International*, *181*(3), 1275–1291. https://doi.org/10.1111/j.1365-246X.2010.04601.x

Sherkati, S., Molinaro, M., Frizon de Lamotte, D., & Letouzey, J. (2005). Detachment folding in the Central and Eastern Zagros fold-belt (Iran): Salt mobility, multiple detachments and late basement control. *Journal of Structural Geology*, *27*(9), 1680–1696. https://doi.org/10.1016/j.jsg.2005.05.010

Talebian, M., & Jackson, J. (2004). A reappraisal of earthquake focal mechanisms and active shortening in the Zagros mountains of Iran. *Geophysical Journal International*, *156*(3), 506–526. https://doi.org/10.1111/j.1365-246X.2004.02092.x

Tatar, M., Hatzfeld, D., & Ghafory-Ashtiany, M. (2004). Tectonics of the Central Zagros (Iran) deduced from microearthquake seismicity. *Geophysical Journal International*, *156*(2), 255–266. https://doi.org/10.1111/j.1365-246X.2003.02145.x

Valkaniotis, S., (2020). A large number of #landslides triggered by the June 9 2020 #earthquake in southern #Iran, mapped using before & after #Sentinel2 images. Landslides, debris falls & avalanches are marked with yellow-red colors. Https://t.co/SyJt3v3be8 [Tweet]. *@SotisValkan*. https://twitter.com/SotisValkan/status/1274433064572157959

Verdon, J. P., Baptie, B. J., & Bommer, J. J. (2019). An Improved Framework for Discriminating Seismicity Induced by Industrial Activities from Natural EarthquakesAn Improved Framework for Discriminating Seismicity Induced by Industrial Activities from Natural Earthquakes. *Seismological Research Letters*, *90*(4), 1592–1611. https://doi.org/10.1785/0220190030

Vergés, J., Saura, E., Casciello, E., Fernàndez, M., Villaseñor, A., Jiménez-Munt, I., & García-Castellanos, D. (2011). Crustal-scale cross-sections across the NW Zagros belt: Implications for the Arabian margin reconstruction. *Geological Magazine*, *148*(5–6), 739–761. https://doi.org/10.1017/S0016756811000331

Wright, T. J., Parsons, B. E., Jackson, J. A., Haynes, M., Fielding, E. J., England, P. C., & Clarke, P. J. (1999). Source parameters of the 1 October 1995 Dinar (Turkey) earthquake from SAR interferometry and seismic bodywave modelling. *Earth and Planetary Science Letters*, *172*(1), 23–37. https://doi.org/10.1016/S0012-821X(99)00186-7

Yeck, W. L., Hayes, G. P., McNamara, D. E., Rubinstein, J. L., Barnhart, W. D., Earle, P. S., & Benz, H. M. (2017). Oklahoma experiences largest earthquake during ongoing regional wastewater injection hazard mitigation efforts. *Geophysical Research Letters*, *44*(2), 711–717. https://doi.org/10.1002/2016GL071685

Zahradnik, J., Jansky, J., & Plicka, V. (2008). Detailed Waveform Inversion for Moment Tensors of M∼4 Events: Examples from the Corinth Gulf, Greece. *Bulletin of the Seismological Society of America*, *98*(6), 2756–2771. https://doi.org/10.1785/0120080124

Zhang, H., Eaton, D. W., Li, G., Liu, Y., & Harrington, R. M. (2016). Discriminating induced seismicity from natural earthquakes using moment tensors and source spectra. *Journal of Geophysical Research: Solid Earth*, *121*(2), 972–993. https://doi.org/10.1002/2015JB012603

Journal of Geophysical Research: Solid Earth

Supporting Information for

The 2019–2020 Khalili (Iran) earthquake sequence — anthropogenic seismicity in the Zagros Simply Folded Belt?

Mohammdreza Jamalreyhani[1,2], Léa Pousse-Beltran[3,4], Pınar Büyükakpınar[5], Simone Cesca[2], Edwin Nissen[3], Abdolreza Ghods[6], José Ángel López-Comino[7,8,9], Mehdi Rezapour[1], Mahdi Najafi[6]

[1]Institute of Geophysics, University of Tehran, Iran.

[2]GFZ German research center for Geosciences, Potsdam, Germany.

[3]School of Earth and Ocean Sciences, University of Victoria, Victoria, British Columbia, Canada

[4]Univ. Grenoble Alpes, Univ. Savoie Mont Blanc, CNRS, IRD, UGE, ISTerre, 38000 Grenoble, France

[5]Kandilli Observatory and Earthquake Research Institute, Boğaziçi University, İstanbul, Turkey.

[6]Department of Earth Sciences, Institute for Advanced Studies in Basic Sciences, Zanjan, Iran.

[7]Instituto Andaluz de Geofísica, Universidad de Granada, Granada, Spain.

[8]Departamento de Física Teórica y del Cosmos, Universidad de Granada, Granada, Spain.

[9]Institute of Geosciences, University of Potsdam, Potsdam-Golm, Germany.

Corresponding author: Mohammadreza Jamalreyhani (m.jamalreyhani@gmail.com)

Contents of this file

Table S3: Information of relocated 115 events of the 2019–2020 Khalili seismic sequence (M_n ≥ 3.0) using multiple-event epicentral relocation technique.
Reference.

Text S1: Details of InSAR inversion of the June 9, 2020 M_w 5.7 Khalili mainshock

We first downsampled the unwrapped line-of-sight displacements, using a Quadtree algorithm to densify data in areas of steep phase gradient around the earthquake (Jonsson et al. 2002). Using the expressions of Okada (1985), we then solved for the minimum misfit strike, dip, rake, surface projection coordinates, length, and top and bottom depths of a rectangular fault plane with uniform 0.5 m slip buried in a half-space with elastic Lamé parameters $\lambda = \mu = 2.5 \times 10^{10}$ Pa, to represent the sedimentary cover (e.g. Nissen et al., 2010, Elliot et al. 2015) In our inversion, each ascending-track interferogram (A130 and A28) was weighted half of the single descending-track interferogram (D64), and we simultaneously solved for ambiguities in their zero displacement levels and residual orbital ramps. The inversion was performed using a nonlinear downhill Powell's algorithm, with multiple Monte Carlo restarts used in order to avoid local minima (Wright et al. 1999). Having established the fault geometry in this way, we then extend the model fault plane along strike and up and down dip, subdivide it into 2 × 2 km patches, and solve for the slip and rake distribution (Funning et al. 2005).

As is commonly the case for buried reverse faulting earthquakes, the dip direction of the causative fault is unclear from the InSAR deformation alone. We therefore explored both SSW- and NNE-dipping model faults (Tables S1–S2), and chose the best model on the basis of which was most consistent with independent seismological results (hypocenter locations and focal mechanisms).

NNE-dipping model fault geometry

In this geometry, inverting the unwrapped interferograms for uniform slip on a single model fault, we obtained a fault with strike 286°, a shallow dip angle of 19°, and a rake of 91° (Table S1 and Figure S11). Solving for distributed slip reproduces the observed deformation well (RMS 7.1 mm), (Figure S12). This InSAR distributed slip model has moment magnitude M_w 5.9.

SSW-dipping model fault geometry

In this geometry, inverting for uniform slip on a single model fault yielded strike 106°, dip 66°, and rake 83° (Table S2 and Figure S13). We used this geometry to produce a distributed slip model (Figure S14), which fits the observed deformation with a RMS of 7.4 mm. An additional distributed slip inversion with variable rake only slightly reduced residual displacements to 7.2 mm, so we prefer the simpler model with distributed slip but uniform rake.

This model left residual fringes around the eastern tip of the fault, motivating us to explore another uniform inversion with two faults (Table S2 and Figure S15). For a stable inversion we needed to reduce the number of free parameters, and we thus fixed the center of the faults using the shape and positions of the observed fringes. This model geometry was then used to solve for distributed slip. The resulting two model faults fit the observations better (RMS 6.5 mm) than a single fault can, and the residual fringes are much reduced. A variable rake model improves the fit only slightly (RMS 6.4 mm), and so we prefer the simpler model, with distributed slip but uniform rake.

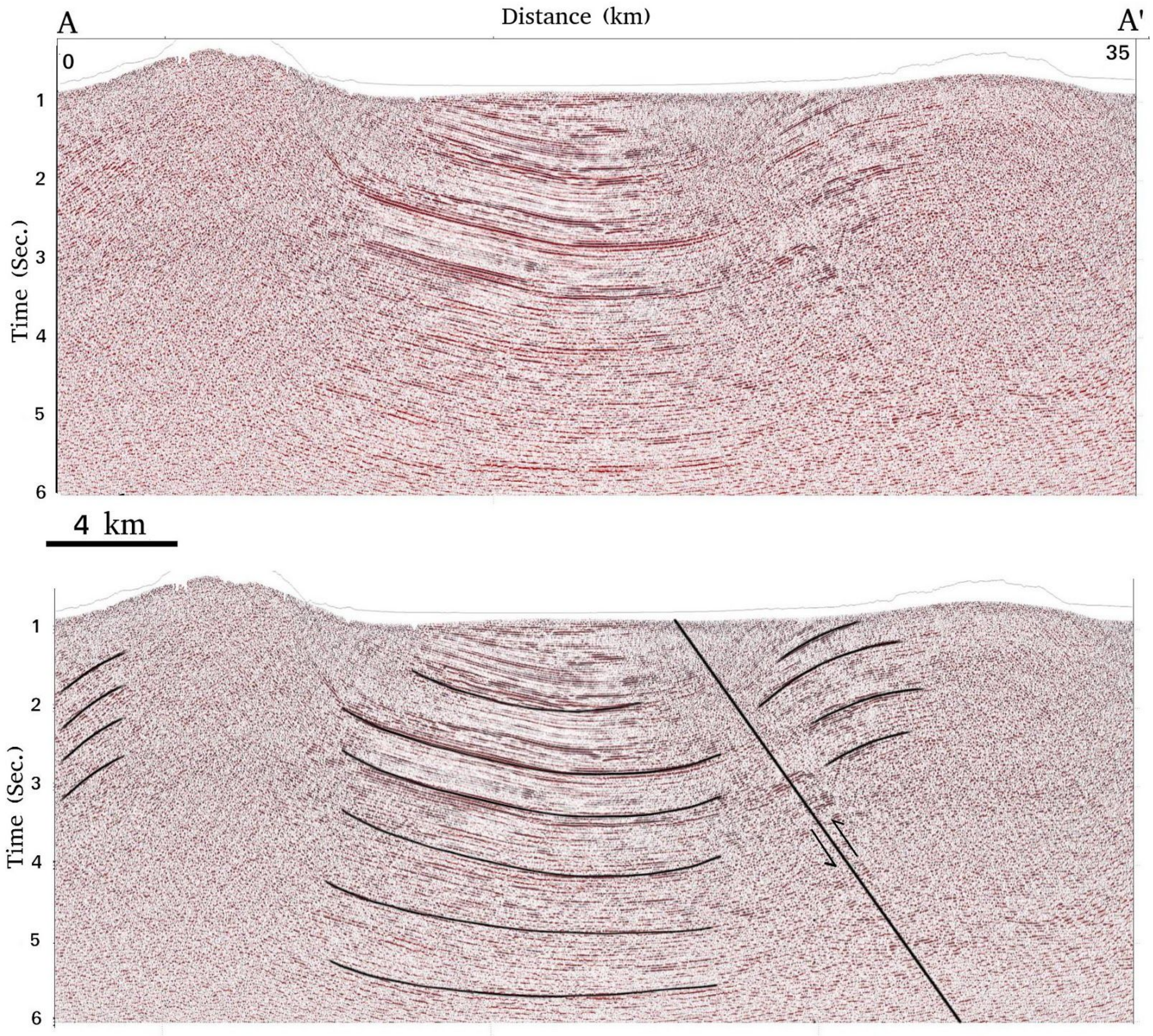

Figure S1. Seismic reflection profile across the central Varavi anticline and western Shanul anticline (profile A–A' in Figure 2). The upper panel is uninterpreted, and the lower panel interpreted with curved lines indicating prominent reflectors and the straight line indicating the approximate location of a N-dipping reverse fault. The y-axis is two way travel time.

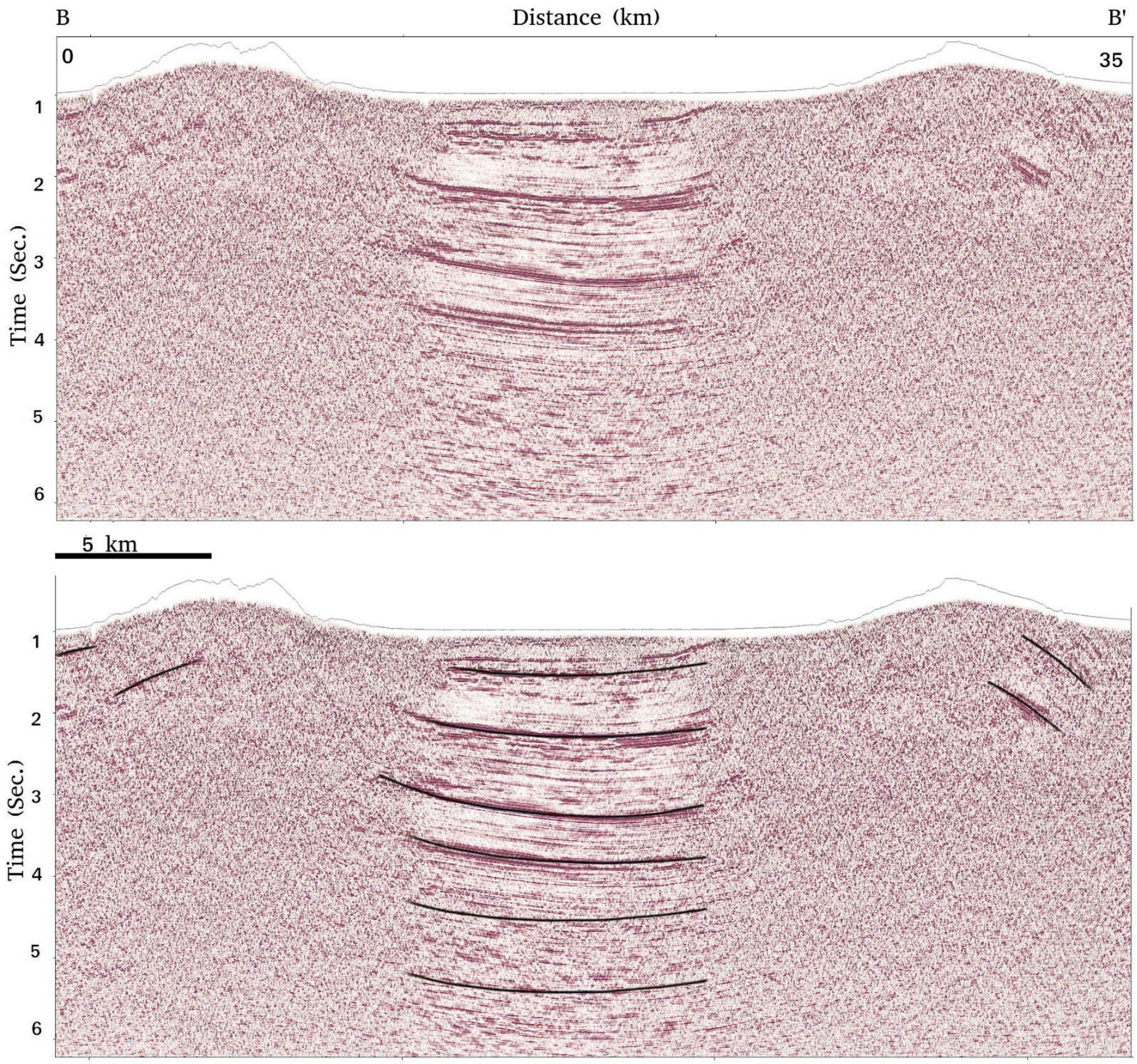

Figure S2. Seismic reflection profile across the eastern Varavi anticline and eastern Shanul anticline (profile B–B' in Figure 2). The upper panel is uninterpreted, and the lower panel interpreted with curved lines indicating prominent reflectors. The y-axis is two way travel time.

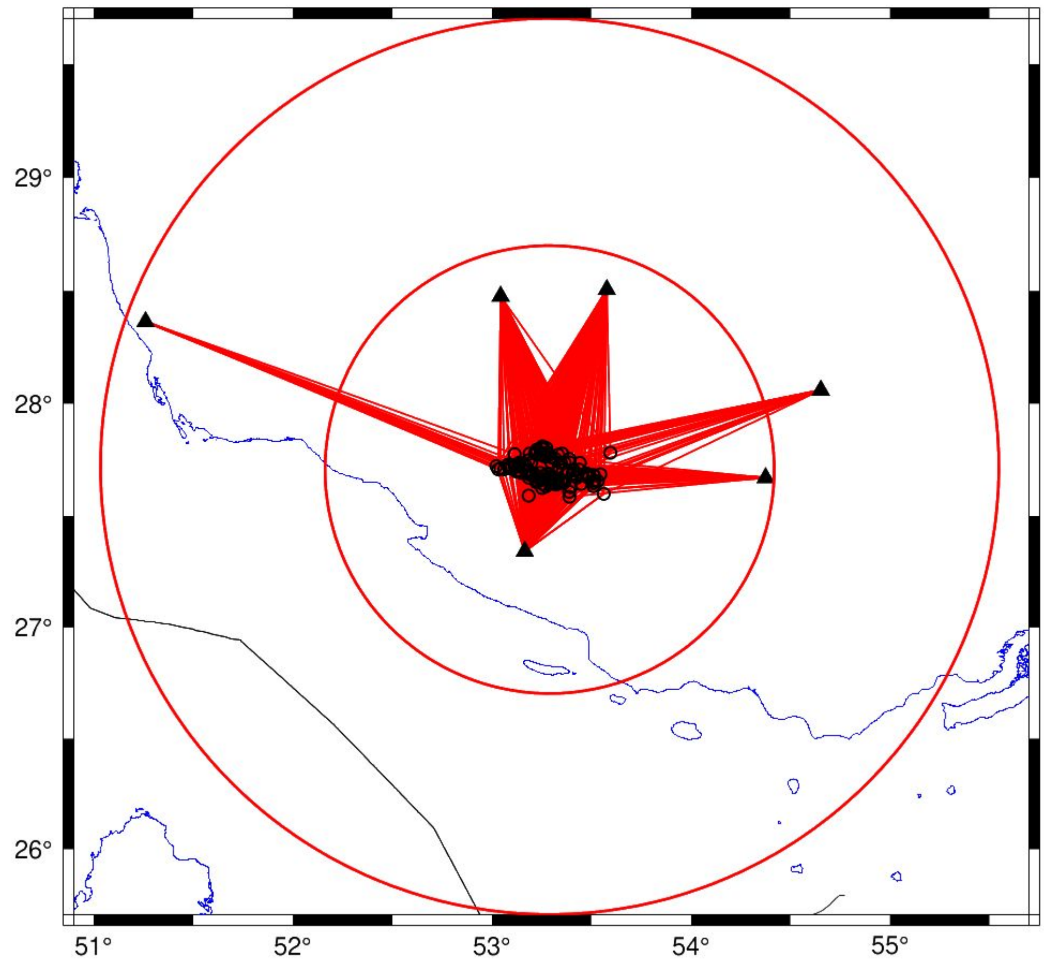

Figure S3. IRSC station distribution (black triangles) and ray paths (red straight lines) used to relocate the 2019-2020 Khalili seismic sequence (black open circles). Large red circles show radii of 100 km and 200 km from the cluster hypocentroid. These stations were also used for moment tensor inversion.

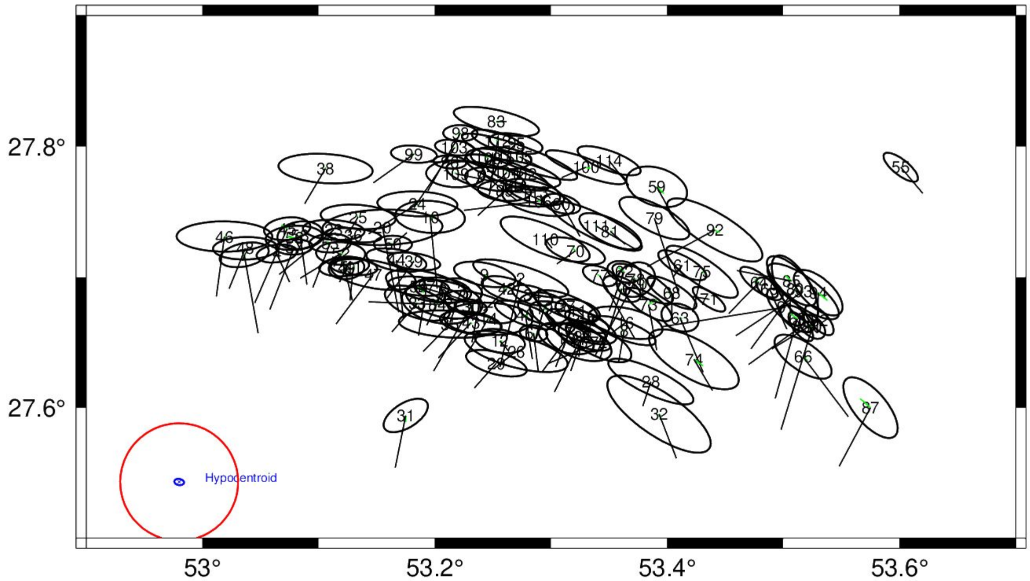

Figure S4. Relocated earthquake hypocenters with 90% confidence ellipses. The hypocentroid uncertainty is shown with the blue confidence ellipse at the bottom left corner. Numbers denote the order of events in the cluster and presented in Table S3.

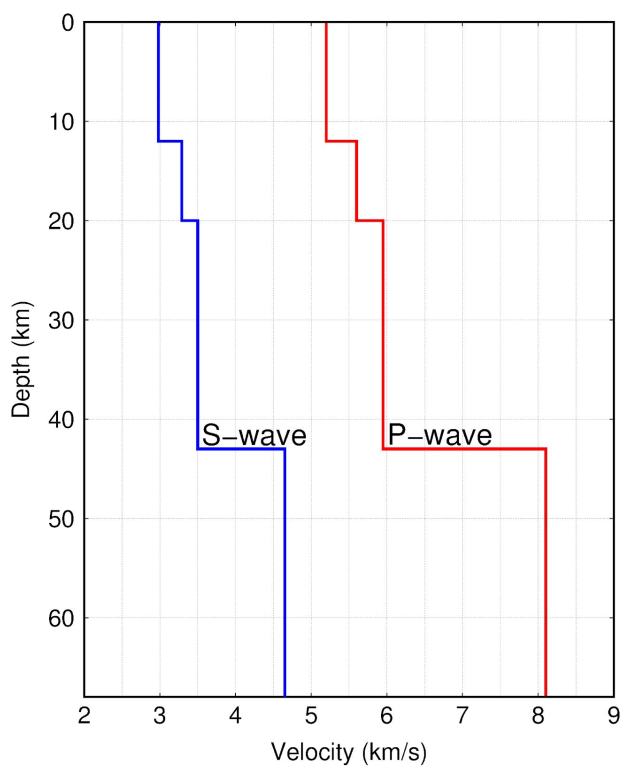

Fig S5. Regional velocity model — modified after Karasözen et al. (2019) — used for multiple-event relocation (to calculate the theoretical travel times presented in Figure S6) and calculating the Green's functions for moment tensor inversion.

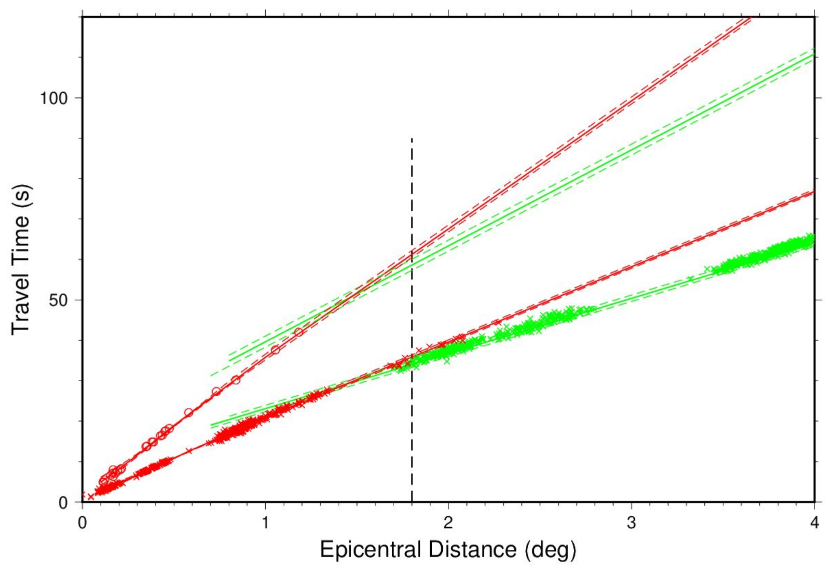

Figure S6. Fit between observed phase arrivals (Pg: Red crosses, Sg: Red circles, Pn: Green crosses) and theoretical travel times (Red and green lines) calculated from the velocity model presented in Figure S5, for epicentral distances of up to 4°.

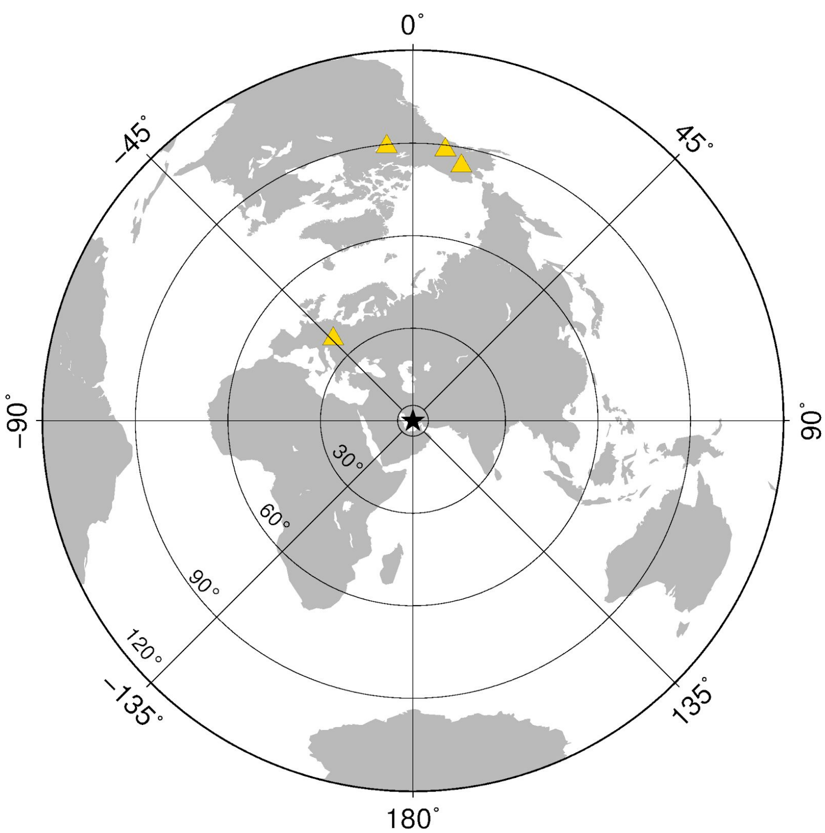

Figure S7. Yellow triangles show four different seismic arrays (BCA, IMAR, YKA, and GERES) used to improve the signal-to-noise ratio for calculation of focal depth from delay between direct *P* and surface reflected *pP* phases. Black star shows the June 9, 2020 M_w 5.7 Khalili mainshock.

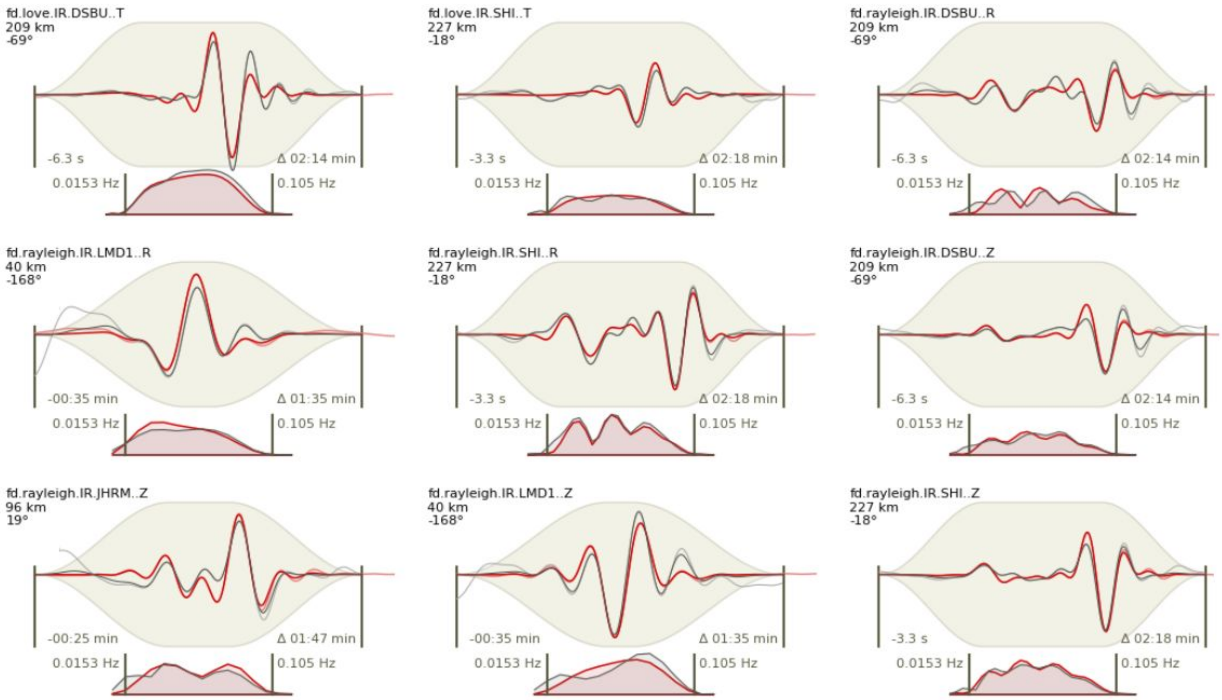

Figure S8. Waveforms fit in time domain and amplitude spectra for the June 24, 2019 M_w 4.2 normal faulting earthquake. Red and black waveforms/spectra show synthetic and observed records, respectively. Numbers within the panels describe the time window and the frequency band. Information to the left of each waveform gives (from top to bottom) the station name, component, distance to the source, and azimuth.

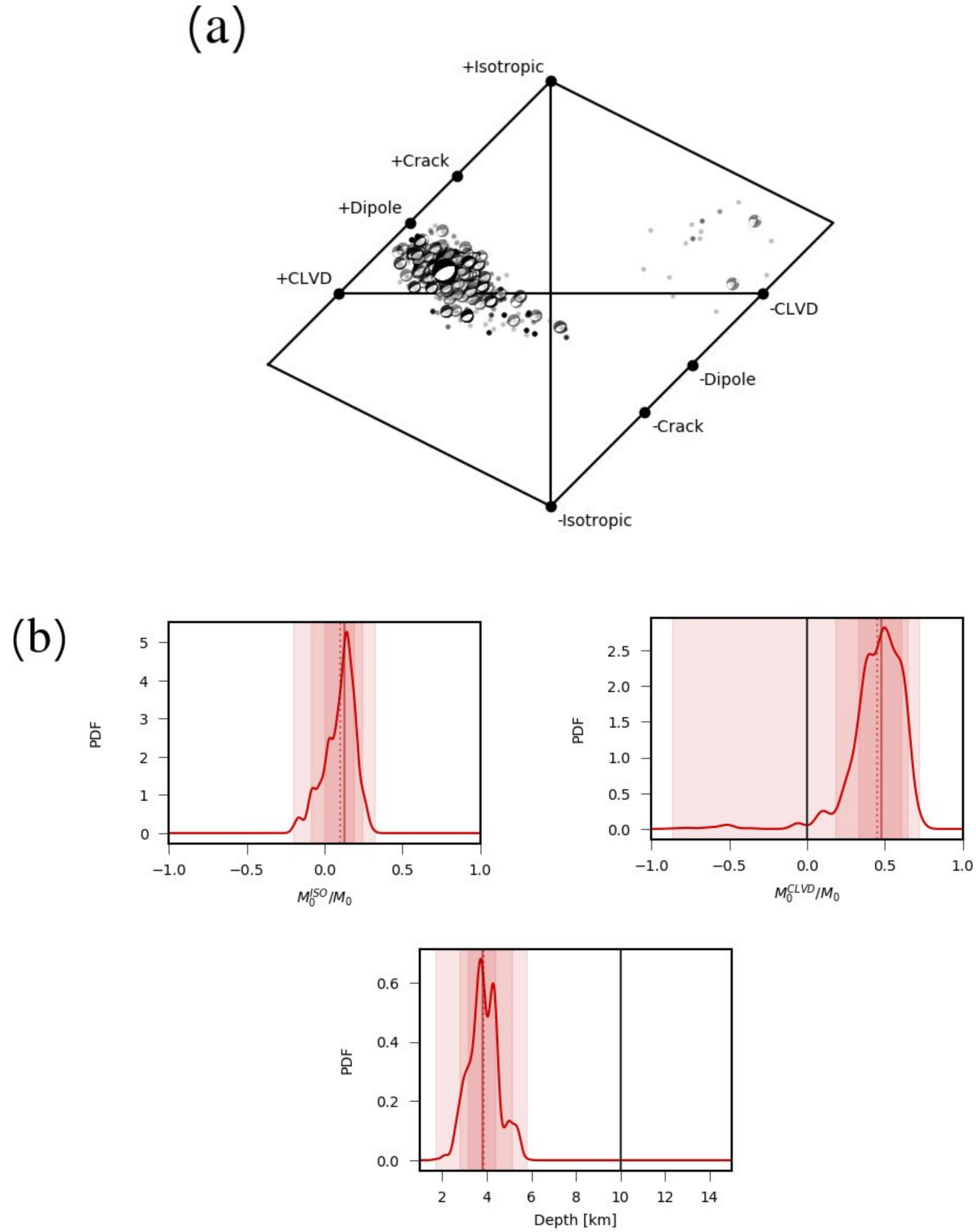

Figure S9. (a) Hudson's source type plot (Hudson, 1989) with the ensemble of bootstrap solutions, for the June 24, 2019 M_w 4.2 normal faulting earthquake. About 10% of the focal mechanisms are shown and others are represented as dots. (b) Probability density functions the CLVD, ISO and centroid depth components for the same earthquake. The plot ranges are defined by the given parameter bounds and (model space). The red solid vertical and dashed lines give the median and mean of the distribution, respectively. Dark gray vertical lines show initial values. The overlapping red-shaded areas show the 68% confidence intervals (innermost area), the 90% confidence intervals (middle area) and the minimum and maximum values (widest area).

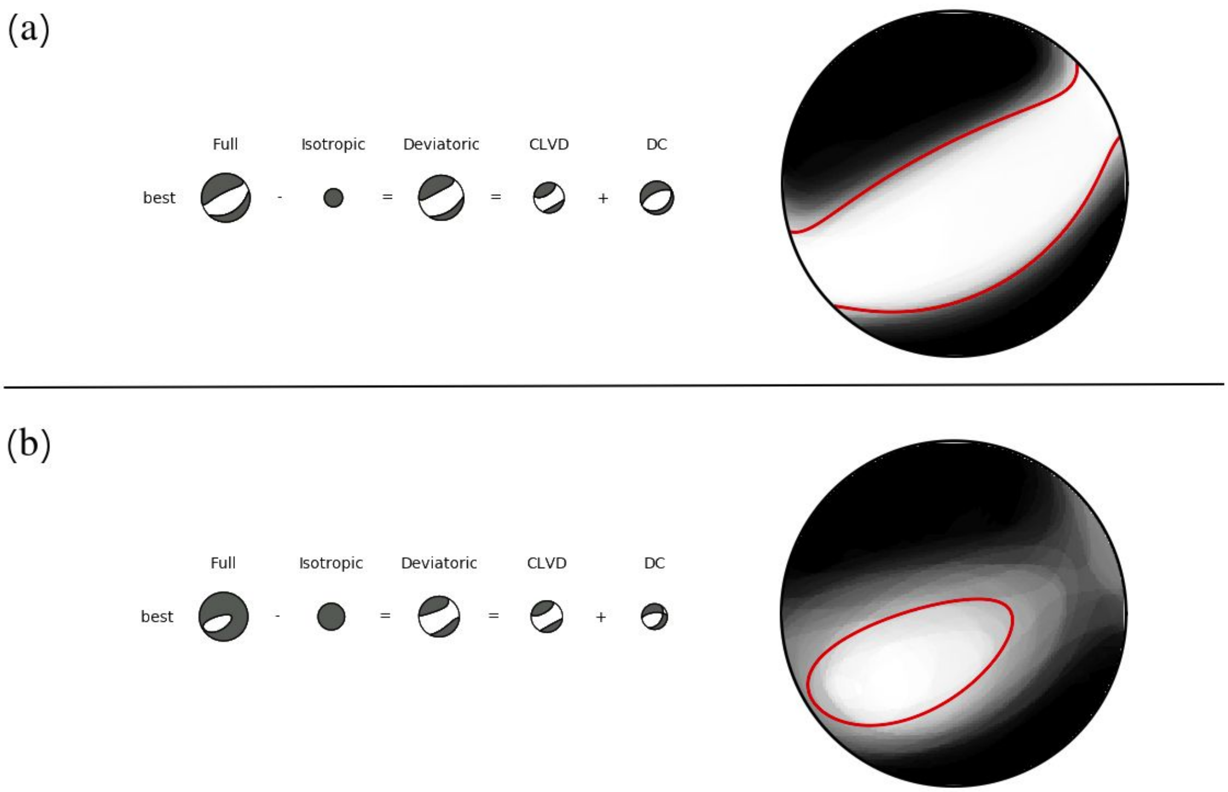

Figure S10. Moment tensor decomposition into isotropic, deviatoric and best double couple components for the two normal mechanisms in the cluster; **a)** the June 24, 2019 M_w 4.2 and **b)** The July 16, 2019 M_w 4.0. The symbol size indicates the relative strength of the components. The fuzzy moment tensors illustrate solution uncertainties. Unfortunately, no independent solution is available in the GCMT catalog or other catalogs for comparison.

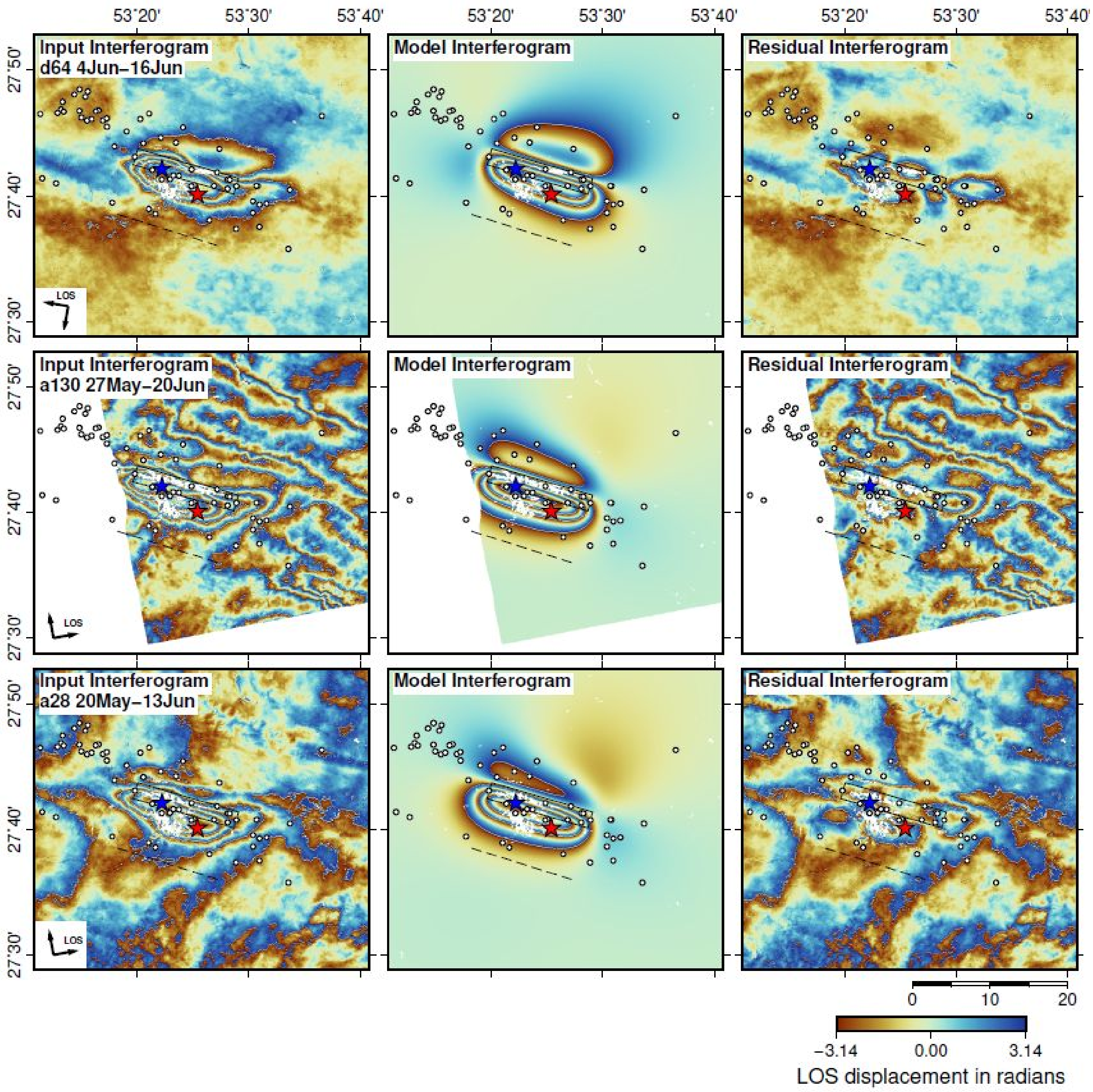

Figure S11. InSAR data (left column), model (middle) and residuals (right) for a single, NNE-dipping model fault with uniform slip (see parameters in Table S1). The three rows show Sentinel-1 tracks D64 (top), A130 (middle), and A28 (bottom). Though we inverted downsampled, unwrapped line-of-sight displacements, interferograms are shown rewrapped in order to accentuate deformation gradients. The dashed black line is the surface projection of the model fault, the black rectangle is the model fault plane outline at depth, and the red and blue stars are the relocated epicenters of the M_w 5.7 mainshock and the M_w 5.4 foreshock, respectively.

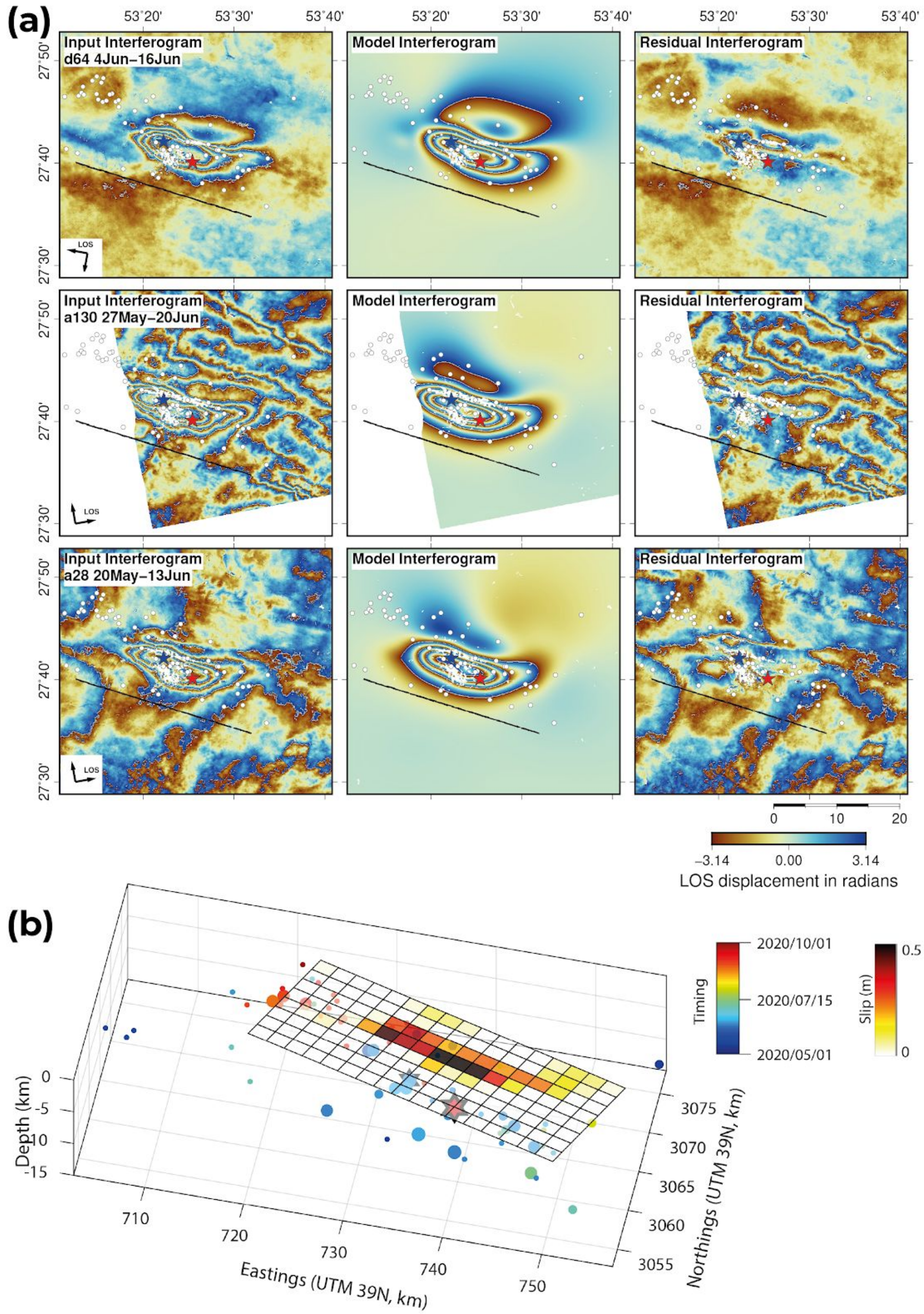

Figure S12. (a) InSAR data (left column), model (middle) and residuals (right) for a single, NNE-dipping model fault with distributed slip. The layout is otherwise the same as in Figure S11. **(b)** Model slip distribution. The model fault is divided into 2 km square patches.

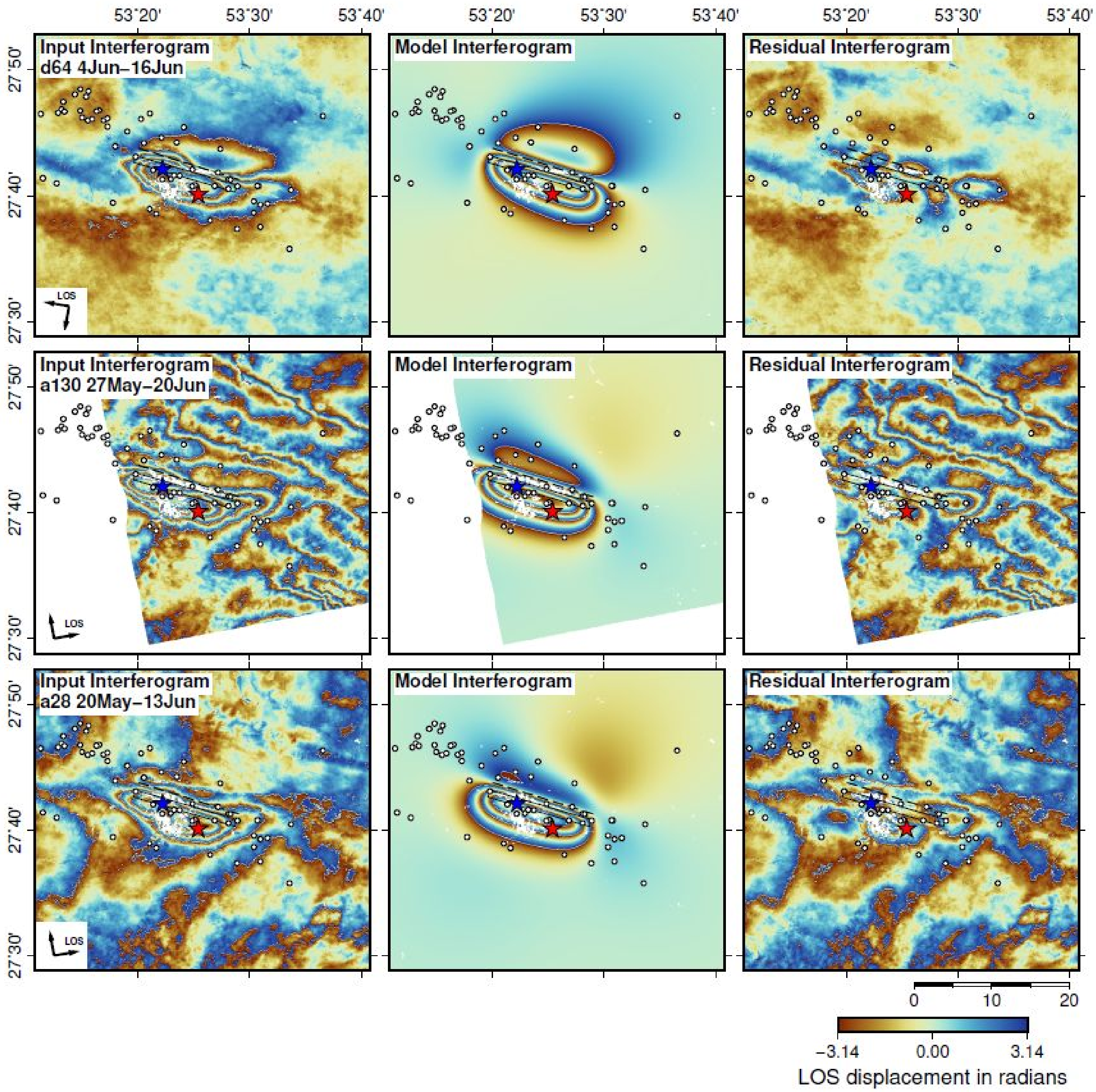

Figure S13. InSAR data (left column), model (middle) and residuals (right) for a single, SSW-dipping model fault with uniform slip (see parameters in Table S2). The layout is otherwise the same as in Figure S11.

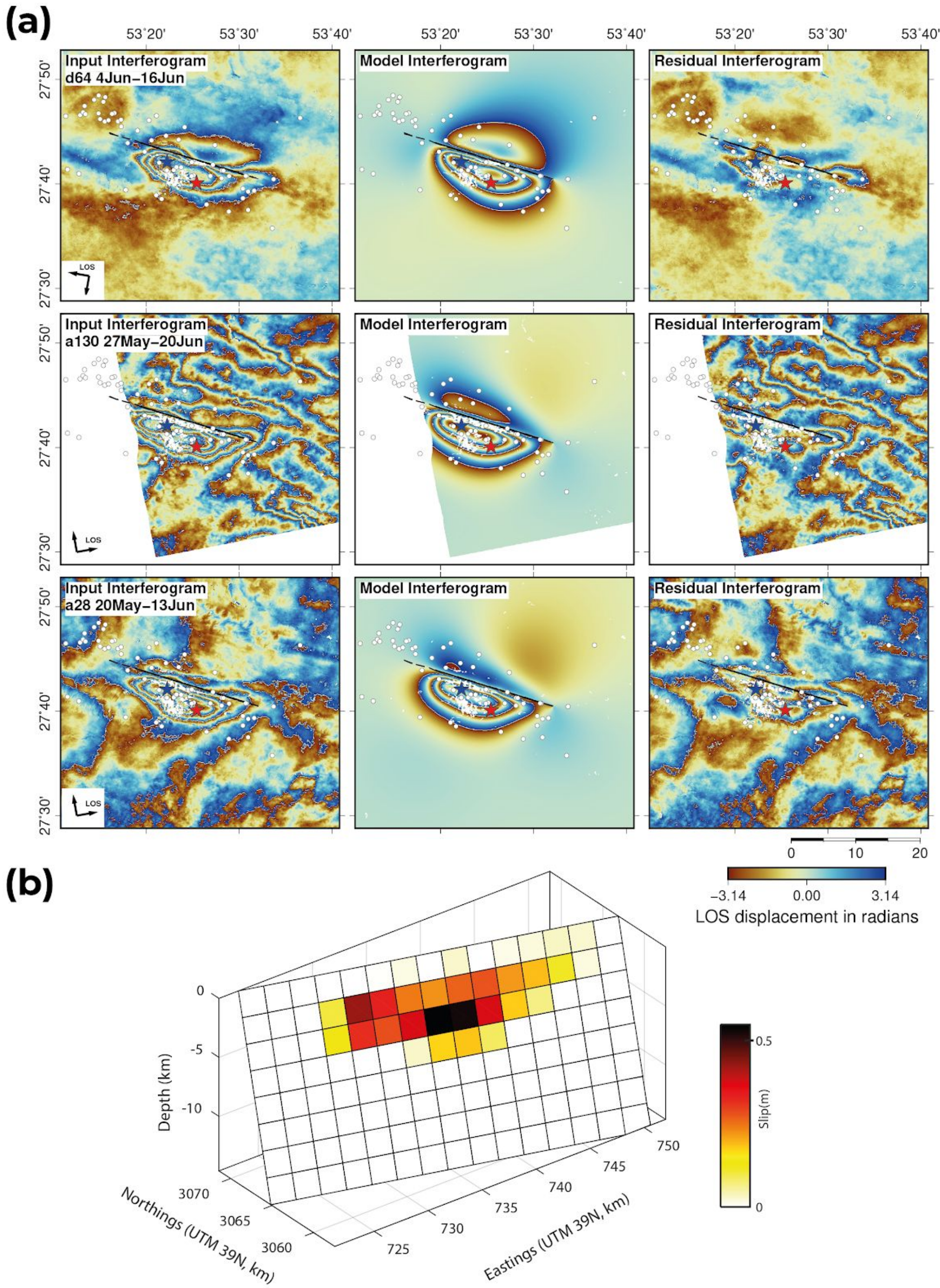

Figure S14. (a) InSAR data (left column), model (middle) and residuals (right) for a single, SSW-dipping model fault with distributed slip. **(b)** Model slip distribution. The model fault is divided into 2 km square patches.

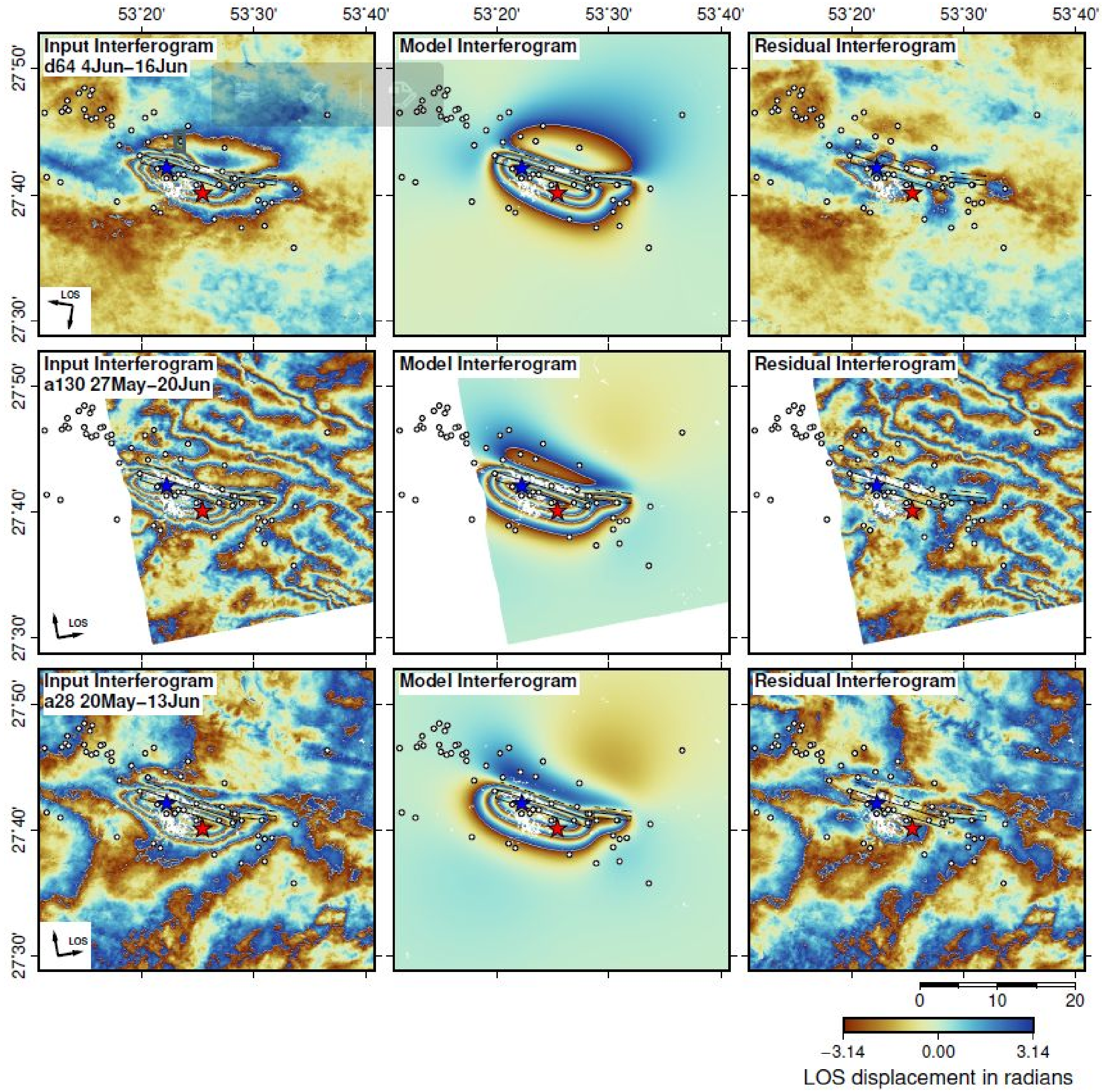

Figure S15. InSAR data (left column), model (middle) and residuals (right) for two SSW-dipping model faults with uniform slip (see parameters in Table S2). The layout is otherwise the same as in Figure S11.

	Probability (%)	Score
Q1: Has there been previous (either historical or instrumental) seismicity at the same site, or within the same regional setting?	100	1
a. Earthquakes have previously occurred in vicinity to the site, with similar rates and magnitudes: −5.		
b. Earthquakes have previously occurred within the same regional setting, with similar rates and magnitudes: −2.		
c. Earthquakes have not occurred at similar rates or magnitudes within the regional setting: +5		
d. Past earthquakes occurred at similar depths within the regional setting: −3.		
e. Earthquakes are significantly shallower than any past events that have been observed within the regional setting: +3.		
Q2: Is there temporal coincidence between the onset of events and the industrial activities?	100	5
a. The earthquake sequence began prior to the commencement of industrial activity: −15.		
b. The earthquake sequence did not begin until a significant period of time after the cessation of industrial activity: −5.		
c. The earthquake sequence began while the industrial activity was ongoing: +5.		
Q3: Are the observed seismic events temporally correlated with the injection or extraction activities?	100	4
a. The earthquakes are coincident with the industrial activity, but there is minimal correlation: −4.		
b. There is some temporal correlation between the seismicity and the industrial activity: +4.		
c. There is strong temporal correlation between the seismicity and the industrial activity (e.g., between rates of injection and rates of seismicity): +15.		
Q4: Do the events occur at similar depths to the activities?	100	3
a. Earthquakes do not occur at the same depth, and there is no plausible mechanism by which stress or pressure changes could be transferred to these depths: −4.		
b. Earthquakes do not occur at the same depth, but plausible mechanisms exist by which stress or pressure changes could be transferred to these depths: +2.		
c. Earthquakes occur at similar depths to the industrial activity: +3.		
Q5: Is there spatial collocation between events and the activities?	100	5
a. Earthquakes are distant to the activities, given the putative causative mechanism: −10.		
b. Earthquakes are sufficiently close to the activities, given the putative causative mechanism: +5.		
c. If earthquake loci change with time, this change is consistent with the industrial activity, for example, growing radially from a well or shifting in response to the start of a new well: +10.		
Q6: Is there a plausible mechanism to have caused the events?	50	1
a. No significant pore-pressure increase or decrease occurred that can be linked in a plausible manner to the event hypocentral position: −5.		
b. Some pore-pressure or poroelastic stress change occurred that can be linked in a plausible manner to the event hypocentral position: +2.		
c. A large pore-pressure or poroelastic stress change occurred that can be linked in a plausible manner to the event hypocentral position: +5.		
Q7: Do the source mechanisms indicate an induced event mechanism?	100	0
a. The source mechanisms are consistent with the regional stress conditions: 0.		
b. Source mechanisms are not consistent with the regional stress conditions, but are consistent with a putative causative mechanism (e.g., thrust faults above a subsiding reservoir): +4.		

Figure S16. Questions, answers with probability and scores for the Khalili seismic sequence according to the framework proposed by Verdon et al. (2019) for discriminating seismicity induced by industrial activities from natural earthquakes. Red text indicates the selected answer to each question. We assign a probability of 50% for question number 6 (Q6), due to lack of accurate pore pressure changes data to verify fully this question.

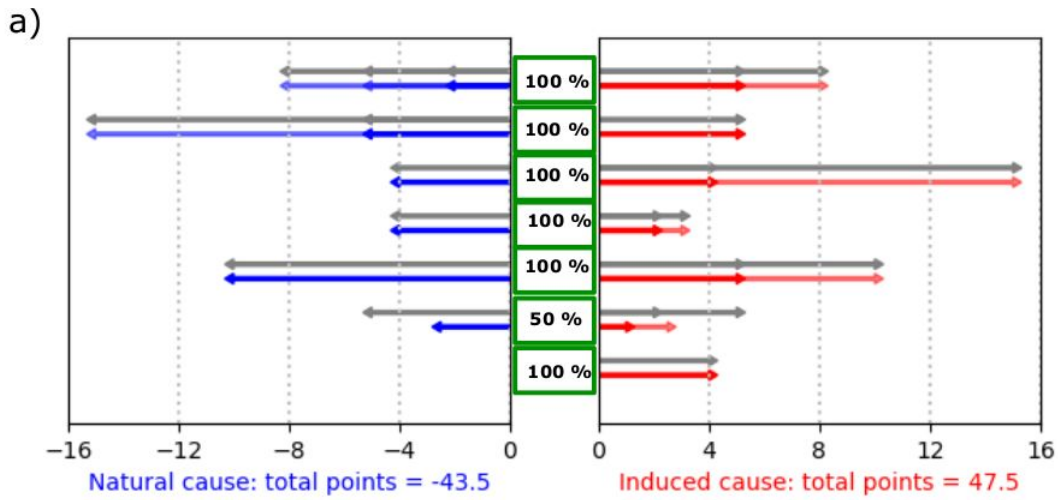

$$ESR = \frac{(|-43.5|+47.5)}{96} \times 100 = 94.8\%$$

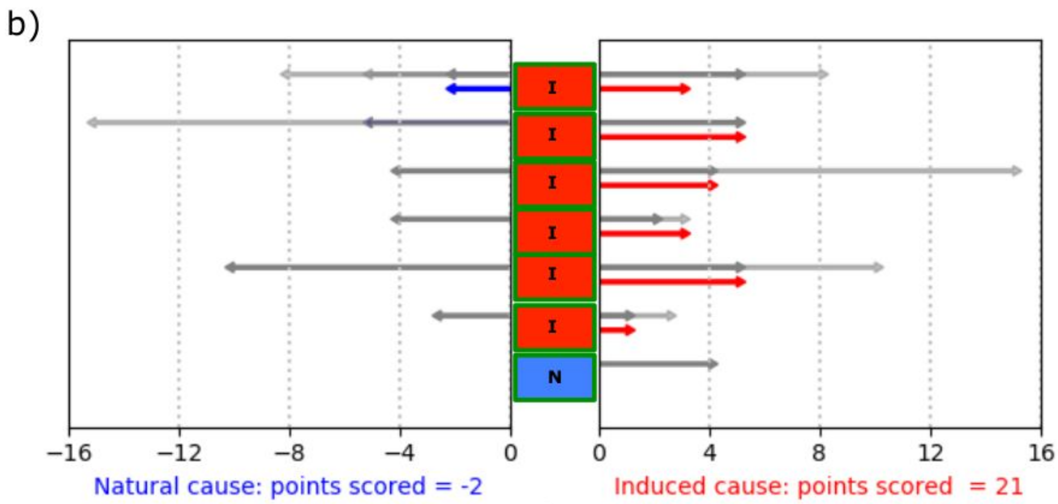

$$IAR = \frac{19}{|47.5|} \times 100 = 40.0\%$$

Figure S17. Schematic illustration of the evidence strength ratio (ESR) and induced assessment ratio (IAR) according to the framework proposed by Verdon et al. (2019) for discriminating the 2019-2020 Khalili seismic sequence is induced or natural. **(a)** ESR, which describes the quality and quantity of information used in the assessment. Grey arrows show the maximum points available for each question (multiple grey arrows in each question represent multiple available answers presented in Figure S16 for each question) and red and blue arrows represent the points for induced (total points = 47.5) and natural (total points = -43.5), respectively. We answer question number 6 by probability of 50%. **(b)** IAR, which categorizes the conclusion regarding the origin of the earthquake inferred from the ESR and decides whether the question and answer points to an induced (I) or natural (N). The points score of the induced and natural are -2 and 21, respectively. For the 2019-2020 Khalili seismic sequence we obtain the IAR and ESR of 40% and 95%, respectively.

Table S1: InSAR model source parameters for a single, NNE-dipping model fault with uniform slip. Eastings and Northings in km are the center of the projected surface break (UTM 39N). The strike, dip, rake, length and top and bottom depths were left as free parameters. To reduce the number of free parameters we fixed the fault slip at 0.5 meters.

Parameters	**Fault 1**
Strike (°)	286
Dip (°)	19
Rake (°)	91
Slip (m)	Fixed 0.5
Eastings (km)	737.6
Northings (km)	3067.3
Length (km)	15.4
Top depth (km)	2.7
Bottom depth (km)	3.5
Moment (Nm)	4.73×10^{17}

Table S2: InSAR model source parameters for (left) one and (right) two SSW-dipping model faults with uniform slip. Eastings and Northings in km are the center of the projected surface break (UTM 39N). The strike, dip, rake, length and top and bottom depths were left as free parameters. To reduce the number of free parameters we fixed the fault slip at 0.5 m or 0.25 m.

Parameters	Single fault		Two faults	
			West Fault	East Fault
Strike (°)	106		108	95
Dip (°)	66		64	66
Rake (°)	83		84	110
Slip (m)	Fixed 0.5		Fixed 0.5	Fixed 0.25
Eastings (km)	734.8		Fixed 737.5	fixed 747.0
Northings (km)	3057.5		Fixed 3067.3	Fixed 3065.8
Length (km)	15.4		14.5	5.4
Top depth (km)	2.4		2.4	1.6
Bottom depth (km)	4.8		4.8	3.2
Moment (Nm)	5.06×10^{17}		4.84×10^{17}	5.91×10^{16}

Table S3: Relocated events of the 2019-2020 Khalili seismic sequence. Date and time are given as year.month.day and hour:minute:second.millisecond format. Lat and Lon are epicentral parameters (latitude and longitude) in degrees. Depth is focal depth (km); **c** represents the fixed depth at 7 km and **n** shows the events with resolved depth by nearby station reading. The order of events (No) is the same as events number in figure S4.

No	Date	Time	Lat	Lon	Depth	Mn
1	2019.2.1	00:1:6.95	27.677	53.239	7.0c	3.3
2	2019.2.1	21:44:35.32	27.699	53.274	7.0c	3.1
3	2019.2.2	05:4:11.55	27.690	53.223	7.0c	3.5
4	2019.2.2	20:25:34.98	27.718	53.064	7.0c	3.7
5	2019.2.6	08:2:40.88	27.708	53.122	7.0c	3.4
6	2019.2.7	16:20:33.16	27.690	53.207	7.0c	3.2
7	2019.2.13	09:19:4.13	27.717	53.036	7.0c	4.0
8	2019.2.15	10:33:28.52	27.659	53.363	7.0c	3.3
9	2019.3.2	11:7:47.09	27.702	53.243	7.0c	3.4
10	2019.3.28	09:11:55.75	27.746	53.196	7.0c	3.3
11	2019.4.2	05:46:4.44	27.674	53.323	7.0c	3.3
12	2019.4.8	21:9:59.80	27.651	53.256	7.0c	3.3
13	2019.4.20	16:56:59.72	27.653	53.313	7.0c	3.4
14	2019.4.20	17:13:49.08	27.668	53.246	7.0c	3.4
15	2019.4.20	18:28:39.09	27.650	53.324	7.0c	3.2
16	2019.4.27	23:13:48.20	27.665	53.364	7.0c	3.1
17	2019.4.28	20:57:16.83	27.666	53.331	7.0c	3.3
18	2019.4.28	22:19:17.79	27.654	53.326	7.0c	3.5
19	2019.4.28	22:25:48.39	27.676	53.294	7.0c	3.5
20	2019.5.10	09:7:54.46	27.738	53.155	7.0c	3.1
21	2019.5.13	23:39:3.53	27.665	53.319	7.0c	3.1
22	2019.5.14	00:0:35.09	27.654	53.327	7.0c	3.1
23	2019.5.26	20:19:46.23	27.736	53.113	7.0c	3.1
24	2019.6.3	08:34:50.77	27.756	53.185	7.0c	3.0
25	2019.6.6	01:17:6.49	27.746	53.134	7.0c	3.3
26	2019.6.12	14:21:18.59	27.643	53.270	7.0c	3.2
27	2019.6.14	08:54:35.89	27.693	53.193	7.0c	3.3
28	2019.6.17	17:29:8.05	27.620	53.386	7.0c	3.1
29	2019.6.23	22:58:20.34	27.634	53.253	7.0c	3.2
30	2019.6.24	15:14:8.01	27.677	53.231	7.0c	4.2
31	2019.6.28	09:8:54.71	27.594	53.175	7.0c	4.2
32	2019.7.5	05:48:51.91	27.595	53.393	7.0c	3.1
33	2019.7.15	20:51:42.00	27.680	53.185	7.0c	3.2
34	2019.7.16	12:2:24.54	27.686	53.284	7.0c	4.0
35	2019.7.19	14:3:23.61	27.664	53.213	7.0c	3.3

No	Date	Time	Lat	Lon	Depth	Mn
36	2019.8.11	20:41:21.54	27.732	53.130	7.0c	3.5
37	2019.8.12	23:28:24.83	27.678	53.313	7.0c	3.0
38	2019.9.19	15:31:11.83	27.783	53.106	7.0c	3.2
39	2019.9.20	15:50:25.50	27.712	53.182	7.0c	3.5
40	2019.10.4	08:43:8.17	27.671	53.279	7.0c	3.6
41	2019.10.5	08:0:20.29	27.708	53.130	7.0c	3.6
42	2019.10.11	22:11:36.95	27.691	53.262	7.0c	3.3
43	2019.11.12	10:3:22.69	27.666	53.231	7.0c	3.2
44	2019.11.13	16:28:20.03	27.713	53.167	7.0c	3.9
45	2019.11.13	17:57:45.58	27.737	53.073	7.0c	4.2
46	2019.11.13	19:46:29.56	27.731	53.019	7.0c	3.3
47	2019.11.13	21:21:33.34	27.702	53.147	7.0c	3.4
48	2019.11.26	07:10:49.55	27.722	53.037	7.0c	3.9
49	2019.12.12	18:26:26.48	27.707	53.125	7.0c	3.1
50	2019.12.22	17:25:19.73	27.725	53.164	7.0c	3.5
51	2019.12.25	02:21:33.34	27.663	53.322	5 n	3.1
52	2020.2.13	13:41:40.27	27.718	53.119	7.0c	3.3
53	2020.2.14	04:11:34.35	27.726	53.110	7.0c	3.5
54	2020.3.21	19:25:23.73	27.693	53.186	10 n	3.1
55	2020.5.12	13:50:51.07	27.784	53.601	7.0c	3.7
56	2020.5.16	18:17:35.55	27.730	53.079	7.0c	3.1
57	2020.5.16	18:20:22.52	27.723	53.079	7.0c	3.4
58	2020.5.16	022:41:8.98	27.732	53.084	7.0c	3.1
59	2020.5.30	22:55:29.39	27.769	53.391	7.0c	3.6
60	2020.5.31	23:59:0.95	27.756	53.309	10 n	4.7
61	2020.6.1	07:41:34.12	27.709	53.413	7.0c	3.3
62	2020.6.9	16:8:48.78	27.704	53.363	7 n	5.4
63	2020.6.9	17:18:12.47	27.669	53.411	7 n	5.7
64	2020.6.9	17:43:17.27	27.696	53.479	7.0c	3.7
65	2020.6.9	19:44:53.53	27.668	53.512	7.0c	4.0
66	2020.6.9	21:55:10.55	27.639	53.517	7.0c	3.3
67	2020.6.9	22:26:58.96	27.657	53.285	9 n	4.1
68	2020.6.9	23:9:38.39	27.688	53.404	4 n	3.0
69	2020.6.10	04:2:26.66	27.691	53.488	7.0c	4.1
70	2020.6.10	5:52:11.26	27.720	53.321	6 n	4.0
71	2020.6.11	2:41:54.88	27.683	53.436	8 n	3.3
72	2020.6.12	3:34:49.82	27.650	53.341	3 n	3.6
73	2020.6.12	04:4:56.48	27.679	53.384	11 n	3.8
74	2020.6.12	13:49:38.88	27.637	53.423	7.0c	3.0
75	2020.6.12	21:34:3.16	27.704	53.430	7.0c	3.1
76	2020.6.13	22:4:14.29	27.691	53.361	7 n	4.8
77	2020.6.13	23:15:3.40	27.701	53.342	10 n	4.6
78	2020.6.14	18:6:0.06	27.698	53.373	14 n	5.2
79	2020.6.15	09:7:49.05	27.745	53.389	7.0c	3.3
80	2020.6.19	06:8:0.15	27.691	53.510	7.0c	3.3
81	2020.6.21	08:5:40.99	27.735	53.351	7.0c	3.8
82	2020.6.23	09:29:58.86	27.667	53.531	7.0c	3.3

No	Date	Time	Lat	Lon	Depth	Mn
83	2020.6.28	23:5:32.02	27.819	53.253	7.0c	3.2
84	2020.7.1	08:45:38.38	27.679	53.202	7.0c	3.3
85	2020.7.3	3:46:41.45	27.697	53.507	7.0c	3.5
86	2020.7.4	9:1:56.79	27.683	53.208	9 n	3.0
87	2020.7.4	09:4:27.09	27.600	53.575	7.0c	3.6
88	2020.7.7	17:40:41.34	27.662	53.515	7.0c	3.3
89	2020.7.10	15:41:37.41	27.766	53.260	7.0c	3.2
90	2020.7.10	20:14:4.57	27.662	53.525	7.0c	4.5
91	2020.7.10	20:22:3.77	27.677	53.502	7.0c	3.1
92	2020.7.13	02:2:34.49	27.736	53.441	7.0c	3.1
93	2020.7.20	14:36:56.20	27.689	53.517	7.0c	3.1
94	2020.7.28	23:10:22.59	27.688	53.530	7.0c	3.6
95	2020.8.21	05:16:3.56	27.802	53.270	7.0c	3.7
96	2020.8.25	12:16:0.10	27.788	53.213	7.0c	4.2
97	2020.8.25	12:25:16.21	27.777	53.244	7.0c	3.4
98	2020.8.31	03:36:50.50	27.810	53.222	7.0c	4.8
99	2020.8.31	05:28:25.13	27.794	53.182	7.0c	3.4
100	2020.8.31	06:1:50.06	27.784	53.330	7.0c	3.2
101	2020.8.31	07:47:6.43	27.769	53.267	7.0c	3.1
102	2020.8.31	10:40:33.14	27.779	53.276	7.0c	3.3
103	2020.8.31	15:57:19.77	27.799	53.217	7.0c	3.7
104	2020.8.31	17:57:49.91	27.780	53.262	7.0c	3.2
105	2020.8.31	21:12:43.35	27.792	53.273	7.0c	3.0
106	2020.9.3	17:30:9.50	27.758	53.289	7.0c	3.2
107	2020.9.4	02:23:50.08	27.695	53.379	7 n	3.1
108	2020.9.8	01:34:17.49	27.791	53.246	7.0c	4.3
109	2020.9.8	02:38:21.55	27.779	53.218	7.0c	3.1
110	2020.9.8	06:5:31.37	27.729	53.295	9 n	3.2
111	2020.9.9	11:27:57.25	27.739	53.339	8 n	3.1
112	2020.9.10	05:10:17.54	27.805	53.254	7.0c	3.2
113	2020.9.19	17:1:33.05	27.765	53.286	10 n	3.5
114	2020.9.21	09:22:12.64	27.789	53.350	7.0c	3.3
115	2020.9.28	03:30:24.22	27.791	53.257	7.0c	3.3

References

Elliott, J. R., Bergman, E. A., Copley, A. C., Ghods, A. R., Nissen, E. K., Oveisi, B., et al. (2015). The 2013 Mw 6.2 Khaki-Shonbe (Iran) Earthquake: Insights into seismic and aseismic shortening of the Zagros sedimentary cover. *Earth and Space Science*, *2*(11), 435–471. https://doi.org/10.1002/2015EA000098

Funning, G. J., Parsons, B., Wright, T. J., Jackson, J. A., & Fielding, E. J. (2005). Surface displacements and source parameters of the 2003 Bam (Iran) earthquake from Envisat advanced synthetic aperture radar imagery. *Journal of Geophysical Research: Solid Earth*, *110*(B9). https://doi.org/10.1029/2004JB003338

Hudson, J. A., Pearce, R. G., & Rogers, R. M. (1989). Source type plot for inversion of the moment tensor. *Journal of Geophysical Research: Solid Earth*, *94*(B1), 765–774. https://doi.org/10.1029/JB094iB01p00765

Jonsson, S., Zebker H., Segall P., Amelung F. (2002). Fault slip distribution of the Mw 7.2 Hector Mine earthquake estimated from satellite radar and GPS measurements. *Bulletin of the Seismological Society of America*. 92, 1377–1389. https://doi.org/10.1785/0120000922.

Karasözen, E., Nissen, E., Bergman, E. A., & Ghods, A. (2019). Seismotectonics of the Zagros (Iran) From Orogen-Wide, Calibrated Earthquake Relocations. *Journal of Geophysical Research: Solid Earth*, *124*(8), 9109–9129. https://doi.org/10.1029/2019JB017336

Nissen, E., Yamini-Fard, F., Tatar, M., Gholamzadeh, A., Bergman, E., Elliott, J. R., et al. (2010). The vertical separation of mainshock rupture and microseismicity at Qeshm island in the Zagros fold-and-thrust belt, Iran. *Earth and Planetary Science Letters*, *296*(3), 181–194. https://doi.org/10.1016/j.epsl.2010.04.049

Okada, Y. (1985). Surface deformation due to shear and tensile faults in a half-space. *Bulletin of the Seismological Society of America*, *75*(4), 1135–1154.

Verdon, J. P., Baptie, B. J., & Bommer, J. J. (2019). An Improved Framework for Discriminating Seismicity Induced by Industrial Activities from Natural EarthquakesAn Improved Framework for Discriminating Seismicity Induced by Industrial Activities from Natural Earthquakes. *Seismological Research Letters*, *90*(4), 1592–1611. https://doi.org/10.1785/0220190030

Wright, T. J., Parsons, B. E., Jackson, J. A., Haynes, M., Fielding, E. J., England, P. C., & Clarke, P. J. (1999). Source parameters of the 1 October 1995 Dinar (Turkey) earthquake from SAR interferometry and seismic bodywave modelling. *Earth and Planetary Science Letters*, *172*(1), 23–37. https://doi.org/10.1016/S0012-821X(99)00186-7